POLYTECHNIC UNIVERSITY OF TURIN
GRENOBLE SCHOOL OF ENGINEERING - PHELMA
SWISS FEDERAL INSTITUTE OF TECHNOLOGY - EPFL

Joint Master's degree in Nanotechnologies for ICTs

Application and exploration of magnetic nanoparticles as magnetic scatterers in magnonic devices

---

Student:
Andrea Mucchietto

External Supervisor:
Prof. Dirk Grundler

Internal Supervisor:
Prof. Sergio Ferrero
Internal Co-supervisor:
Prof. Luciano Scaltrito

September 2018
Polytechnic University of Turin
Department of Electronics and Telecommunications
Academic year 2017–2018

Abstract

Spin waves (magnons) are collective spin excitations in magnetically ordered materials. If exhibiting sub-100 nm wavelength they could become the information carrier of future non charge-based information technology. Due to wavelength mismatch the coupling between magnons and electromagnetic waves at the same frequency is however weak. Efficient microwave-to-magnon transducers are therefore required. Grating couplers making use of nanostructured magnets are a promising route.

Spin waves (SWs) in 100 nm thick yttrium iron garnet (YIG) film are investigated. Colloidal suspensions of magnetic nanoparticles featuring different diameters (in the range of tens of nm) and magnetic behavior (superparamagnetic and ferrimagnetic) are prepared and then deposited by drop-casting on yttrium iron garnet surface. Using integrated microwave antennas spin wave resonance is studied with all electrical spin wave spectroscopy and Brillouin light scattering spectroscopy. Experimental results suggest an enhancement of the inhomogeneous broadening that is attributed to scattering at the deposited nanoparticles.

Contents

1. Motivation and Introduction

The research activity for this master's thesis has been carried out at the Laboratory of Nanoscale Magnetic Materials and Magnonics (*LMGN*) at the Swiss Federal Institute of Technology in Lausanne (*EPFL*).

Magnon excitation and detection in nanoparticles decorated yttrium iron garnet is the main subject of this master's thesis.

In this chapter a general overview of the emerging spin wave based technology is presented.

Current semiconductor electronics for digital and analog application has been facing severe limitations that are imposed by (i) dimensional scaling and (ii) power consumption. Throughout the years technology boosters have been conceived to:

- improve mobility: e.g. strained channel, new channel materials such as III-V n-type
- improve electrostatics: e.g. gate all around (GAA) geometry
- improve subthreshold swing: e.g. tunnel field effect transistor

In addition high k-dielectrics have been investigated to reduce power leakage through gate oxide . Nonetheless miniaturization and power consumption have to comply to fundamental physical limits [Mei00]:

- thermodynamics: limit of energy transfer $E_{min} = \kappa_B T \cdot ln(2)$
- quantum mechanics: Heisenberg's principle defines a lower limit for the power-delay relation
- electromagnetics: finite time for electromagnetic wave to travel along interconnects

Reducing costs for market competitive products leads to high level of device integration demand. Structural scaling down is further motivated by the latest technological shift towards wearable and wireless devices. This need is also fueled by the onset of the 'Internet of Things'. Shrinking down to the nm-scale device structure requires state-of-the-art nanofabrication which ensures a reliable and repeatable process that can be applied to large scale production. Shrinking down devices to the nm-scale is therefore affected by process variability. Noise and parasitics minimization become important issues as well.

Reduction of power consumption is also a key technological driver for next-generation devices, bearing major impact on the autonomy of mobile and portable electronics. Nevertheless this represents an issue in CMOS electronics as heat dissipation and electrical leakages increases power supply.

In this scenario of hampered growth for conventional semiconductor-based electronics a technological paradigm change has the potential to provide us with a solution.

Non charge based beyond CMOS technology has been gaining momentum as research has been done on how to master and exploit magnetic proprties of nanostructured materials for data processing and signal transmission [Chu00]. Within this framework, *Magnonics* is the research field in nanomagnetism that studies spin waves and how to generate, control and detect them. Spin waves (SW), also referred to as *magnons*, are collective spin excitations in a magnetically ordered materials. In analogy to the case of lattice vibration quanta (i.e. phonons) and light quanta (i.e. photons) the bosonic quasiparticle that represents quanta of these wave-like magnetization excitations is known as magnon.

Bloch initiated the scientific research on the physics of spin waves [Blo00]. He was the first to analyze the low temperature spin wave spectrum and thermodynamics of a ferromagnet. Then Kittel and Herring developed a phenomological spin wave theory neglecting magnon-magnon interactions [Her00]. Spin waves interactions were also studied, following different approaches by Holstein and Primakoff [Hol00] and separately by Dyson [Dys00].

The rapid growth of nanotechnology and materials science has allowed for experimental investigations of the application of spin waves to nanoscale devices [Gru00]. Spin waves transfer angular momentum without transporting charge. Spin wave frequencies range from few GHz to THz [Gur00], moreover SW dispersion relation and propagation depends on both materials and external parameters [Gur00], [Ver00]. Magnons can exhibit large group velocity ($\gtrsim$ 20 km/s, [Yu00]) and sub-100nm wavelength [Yu01], [Liu00]. With modern state-of-the-art nanofabrication and nanocharacterization tools magnetic materials can be nanoengineered. Tailoring nanostructures' properties enables better control on spin wave propagation and it explores solutions to extend spin wave lifetime and maximize spin wave propagation length. Spin waves feature exponential decay therefore materials optimization to minimize damping plays an important role.

The magnetic analog of photonic crystal is called *magnonic crystal* (MC). This artificial system can be engineered in 1D, 2D and 3D. Magnonic crystals feature spatially modulated material parameters or periodically changing material composition. Because of the ability to fine-tune their structural and magnetic properties, they offer unrivaled control on spin wave dispersion relation and propagation [Kra00]. MCs can be reconfigured and this fuels even more the scientific and technological interest for magnetic nanostructures as future building blocks for non charge based reprogrammable devices [Ver00]. Reprogrammability is a remarkable feature of magnetic nanosystems and it is widely investigated. Optical reconfiguration for magnetic materials has been experimentally proven [Vog00] and reconfigurable waveguide design for low power spin wave manipulation has been already proposed and experimentally investigated [Hal00].

Scientific research has already achieved seminal works towards a deeper understanding of magnon manipulation and microwave properties of magnetic nanostructures. Magnonics is currently exploring theoretically and experimentally main device concepts and has already achieved prototypes: magnon transistor [Chu01], resonant microwave-to-magnon transducer [Au00], spin wave multiplexer [Vogt00] and majority gate [Fis00].

So far it has been discussed that spin waves have the following advantages for being the next-generation information carrier:

- scalability
- reduced power consumption/dissipation
- multifunctional operation in GHz and THz regime
- nonlinear effects to be used for signal gating, amplification and mixing [Khi00]
- nonreciprocity to be used in microwave devices as circulators and isolators
- wave-like processing of signal (e.g. interference and diffraction)
- reprogrammability

Despite the aforementioned advantages of magnons control for data processing there are still big challenges to be addressed:

(i) improve excitation efficiency for short-waved magnons

(ii) interface with existing microwave electronics

This master's thesis is dedicated to explore novel solutions to issue (i), i.e. increase spin wave generation efficiency. For this reason the last part of this chapter will be devoted to develop further critical points relating to (i).

A perturbation needs to be created in order to trigger coherent spin precessional motion. Mechanisms to excite spin waves have been studied, the focus is nowadays on optimizing SW generation efficiency. SW generation methods are various, here only few should be cited: (i) optical excitation with femtosecond laser pulses [Sav00], (ii) SW generation by means of surface acoustic waves (SAWs) [Li00] and (iii) excited by microwave field of a radiofrequency (RF) antenna [Vla00]. This latter mechanism is of particular interest for this thesis.

A microwave antenna can excite spin waves in the medium. Injecting RF signal into the microwave antenna creates a RF magnetic field that interacts with spins in a magnetically ordered material such as ferro- or ferrimagnet. More details will be provided in chapters 2 and 4.

For now it is sufficient to highlight that the existing challenge is to improve *microwave-to-magnon coupling efficiency.* This parameter is limited by the system structure, as the microwave antenna determines the resonant mode's wavelength. To enhance coupling efficiency between long wavelength eletromagnetic waves and magnons a concept from integrated optics and photonics has been introduced in magnonics: the grating coupler effect. The magnonic grating coupler (MGC) effect has been experimentally realized in a nanodevice featuring integrated microwave antennas for spin wave excitation [Yu02]. We will discuss the MGC in section 2.5.2.

Grating coupler effect is determined by a spatial modulation of magnetic susceptibility and dynamic magnetic field. This is engineered by fabricating periodically nanopatterned structures on a ferrimagnetic thin film. This periodic array of nanostructures can be seen as a 2D periodic lattice and can be fabricated with materials.

This lattice provides the high wave-vector modes and strengthens the signal corresponding to grating coupler induced spin wave resonance. This work is important because it gives a top down approach solution to magnon generation efficiency issue. It also highlights the physical parameters that are essential for pushing the optimization of this effect ahead:

- lattice constant of the array should be as small as possible
- filling factor of the periodically spaced nanostructures should be large

To overcome limitations provided by top-down-nanolithography magnetic nanoparticles come into play as potential magnon nanoemitter. The size of nanoparticles can be as small as a few nanometers thus overcoming nanolithography limitations. This is ideal in the attempt to continue scaling down the wavelength of the excited spin wave.

In this thesis we address this route for coupling enhancement and wavelength downconversion. We explore how magnetic nanoparticles modify magnetization dynamics of 100 nm thick yttrium iron garnet (YIG) film. Thereby we analyze the coupling between magnetic nanoparticles and magnons. Targeting the generation of high frequency modes ($\gtrsim$ 50 GHz) hexaferrite-based nanomaterials are also studied in terms of their interaction with excited magnons in 100 nm thick YIG layer.

Organization of the thesis

Chapter 2 provides the reader with a theoretical background on ferromagnetism and spin waves. Chapter 3 presents the experimental techniques and setups that were use during this work. Chapter 4 lays out sample structure and geometry. Chapter 5 introduces nanoparticles that have been processed during the master's thesis work, giving information on magnetic and structural properties. Chapter 6 presents and discusses experimental data. Chapter 7 summarizes the entire work with final comments thus highlighting critical points for future research.

2. Theoretical background

A general description of ferromagnetism and energy contributions in a magnetic system is hereby given. Magnetization dynamics theory and spin wave resonance will be analyzed highlighting key relations.

Micromagnetism is a quasi-classical theory. Based on a theory of continuum magnetization processes are modeled on a characteristic scale length that (i) is large enough to approximate atomic spins with a continous function of position (ii) and at the same time such small to investigate magnetization transition over magnetic domains. The assumption of micromagnetic formalism are [Exl00]:

- Use of classical vectors instead of quantum mechanical operators
- Magnetization length $|\vec{M}|$ is constant in time and space within the investigated sample. It only depends on temperature
- Temperature is constant in time and space
- Free energy is function of magnetization unit vector
- Energy terms are calculated from phenomenological models or replacing with continuum models the atomistic ones.

Micromagnetic approach is used for theoretical discussion.

The concise description that follows has been inspired by a selective reading of textbooks [Gur00], [Blu00], [Sta00], [Sto00].

2.1 Static magnetism

First criterion to classify materials according to their magnetic behavior is the presence of atoms/ions with permanent magnetic moments in their crystal structure. Second criterion, that applies to materials displaying atoms/ions with permanent magnetic moments, is whether they exhibit long-range order.

2.1.1 Susceptibility

For the case of magnetically ordered materials, different arrangements of magnetic moments are observed. Magnetic systems' behavior using macroscopic quantities can be described as follows:

$$\vec{M} = \overleftrightarrow{\chi} \cdot \vec{H} \tag{2.1}$$

With $\vec{M}$ being the net macroscopic magnetic moment per unit volume, $\vec{H}$ the applied field. The quantity $\overleftrightarrow{\chi}$ is the magnetic susceptibility tensor. Susceptibility becomes a scalar for isotropic systems. For this case χ can be used to directly classify magnetic response of a material:

- $\chi < 0$, *diamagnetism.* Materials possess no atoms or ions with permanent magnetic moments. Microscopic Lenz's law can be applied to explain the response of a diamagnetic material to an external applied field. Due to modification of electron orbital motion this material repels the external field.
- $\chi > 0$, *paramagnetism.* Materials have permanent magnetic moments but no long-range order at equilibrium. An external applied field induces a net magnetization, magnetic moments partially align along the direction of the external field. Paramagnets restore their magnetic equilibrium configuration once the external applied field is switched off.
- $\chi \gg 0$, *ferro-* and *ferrimagnetism.* Ferro- and ferrimagnets exhibit a net spontaneous magnetization, i.e. non-zero magnetization at zero external applied field. At zero applied field these magnetic moments might be arranged with different orientation in different region, i.e. *magnetic domains.* Each magnetic domain features a non zero magnetization, the orientation of magnetic domains is such that magnetostatic energy is minimized. Ferrimagnets can be described as the combination of two ferromagnetic sublattices with opposite but different absolute magnetization so that magnetic moments do not cancel out. Ferrites are an example of ferrimagnetic materials. Ferrimagnetic materials can be treated as ferromagnets in the microwave regime.

  Above a critical temperature (Curie temperature T_C for ferromagnets and Néel temperature T_N for ferrimagnets) materials become paramagnetic.
- $\chi > 0$, *antiferromagnetism.* Antiferromagnets can be thought as two interpenetrating sublattices with ferromagnetic order and opposite spontaneous magnetization. Above critical temperature (Néel temperature T_N) antiferromagnets become paramagnetic.

Ferrites and magnetic garnets are very important materials for applications in microwave devices. In the field of magnonics yttrium iron garnet ($Y_3Fe_5O_{12}$, YIG) is the material with the lowest damping for spin waves propagation ($< 1 \cdot 10^{-4}$ [Hau00]). YIG is a ferrimagnet.

2.1.2 Total energy and effective field

Long range magnetic order originate from quantum mechanical exchange interaction. Within a magnetic material different type of interactions are observed and their competition establishes the ground state of system.

Exchange interaction

Exchange interaction determines spontaneous magnetic order in materials. It is explained by Coulomb interaction and Pauli exclusion principle. As a quantum-mechanical interaction it can be modelled according to Heisenberg Hamiltonian:

$$\hat{\mathcal{H}}_{ex} = -\sum_{i,j} J_{ij} \hat{\vec{S}}_i \cdot \hat{\vec{S}}_j \tag{2.2}$$

$\hat{\vec{S}}_p$ is the spin operator relating to the magnetic moment localized at the generic p^{th} lattice site. J_{ij} quantifies the coupling strength between i^{th} and j^{th} positions.

Calculations to reach a quasiclassical formula for exchange starting from quantum mechanical model is provided in [Blu00].

In the continuum limit the exchange energy density can be expressed as:

$$\mathcal{E}_{\text{ex}} = \frac{A}{V} \int [(\vec{\nabla} m_x)^2 + (\vec{\nabla} m_y)^2 + (\vec{\nabla} m_z)^2] d\vec{r}, \tag{2.3}$$

with A being the exchange constant and $\hat{m} = (m_x, m_y, m_z)$ the magnetization unit vector.

Considering nonhomogeneity of the magnetization and of the exchange constant the exchange field is given by [Kra01]:

$$\begin{aligned} \vec{H}_{ex}(\vec{r}, t) &= (\vec{\nabla} \cdot \lambda_{ex}(\vec{r}, t) \vec{\nabla}) \vec{M}(\vec{r}, t), \\ \text{with} \qquad \lambda_{ex} &= \sqrt{2A/(\mu_0 M_{\text{S}}^2)}, \end{aligned} \tag{2.4}$$

with M_{S} referring to saturation magnetization of the system. Epression 2.4 for exchange field will appear later in this theoretical chapter.

Demagnetization field

Demagnetization is caused by long range dipole-dipole interaction. It leads to shape anistropy as it depends on sample geometry. Demagnetization field $\vec{H}_{\text{D}}$ can be worked out from magnetostatic Maxwell's equation:

$$\begin{aligned} \mu_0 \vec{\nabla} \cdot (\vec{H}_{\text{D}} + \vec{M}) &= 0, \\ \vec{\nabla} \times \vec{H}_{\text{D}} &= 0. \end{aligned} \tag{2.5}$$

Eq. 2.5 suggests that demagnetization field can be written as gradient of a scalar function, i.e. the magnetostatic potential ψ:

$$\vec{H}_{\text{D}} = -\vec{\nabla} \psi. \tag{2.6}$$

The demagnetization field following 2.5 is connected to the magnetization. It can be expressed as:

$$\vec{H}_{\text{D}} = \overleftrightarrow{N} \cdot \vec{M}. \tag{2.7}$$

$\overleftrightarrow{N}$ is the demagnetization tensor. Several works have focused on calculating demagnetizing factors for different geometries e.g. thin films [Kali00], ellipsoid [Osb00], rectangular prisms [Aha00].

Combining Eqs 2.5 and 2.6 we can write the Poisson equation for the magnetostatic potential:

$$(\vec{\nabla} \cdot \vec{\nabla}) \psi = -\vec{\nabla} \cdot \vec{M}. \tag{2.8}$$

Exploiting Eq. 2.8 the volume density of magnetic charge can be defined as $\rho_M = -\vec{\nabla} \cdot \vec{M}$. Solving Eq. 2.8 provides an expression of the demagnetization tensor in term of the Green's function ([Neu00], [Hub00]) but this goes beyond the purpose of this theoretical introduction.

In a continuum model the energy density concerning demagnetization effect is described as follows:

$$\mathcal{E}_{\text{D}} = -\frac{\mu_0}{2V} \int_V (\vec{H}_{\text{D}} \cdot \vec{M}) dV. \tag{2.9}$$

Anisotropic magnetic interactions

Anisotropy can be determined by dipolar interaction as in the case of shape anistropy. There are other sources of magnetic anisotropy as well. Magnetocrystalline anisotropy is explained by spin-orbit interaction. Other forms of anisotropy can be electrically and/or thermally induced [Gur00].

Magnetocrystalline anisotropy describes interactions that change according to orientation with respect to crystal lattice axes. Adopting a phenomenological model anisotropy can be written in power series of $\vec{M}$ projections onto crystal axes.

For uniaxial ferromagnets the following approximated formula can quantify the anisotropy energy [Gur00]:

$$\mathcal{E}^{an}_{\text{uni}} = K_1 sin^2(\theta) + K_2 sin^4(\theta) + K_3 sin^6(\theta) + ... \tag{2.10}$$

With K_i $(i = 1, 2, 3, ..)$ being dimensional constants and θ the angle between magnetization direction and main lattice axis. Truncating the power series at first non vanishing term one can identify two situations: (i) for $K_1 > 0$ the crystal axis for which $\theta = 0$ is the easy axis, (ii) for $K_1 < 0$ the crystal axis for which $\theta = 0$ is the hard axis. Eq 2.10 can be rewritten after truncation as:

$$\mathcal{E}^{an}_{\text{uni}} = -K_u(\hat{m} \cdot \hat{e}_u)^2 \tag{2.11}$$

$\hat{e}_u$ is the unit vector indicating main axis and $\hat{m}$ is the magnetization unit vector. The corresponding anisotropy field can be written as [Gur00]:

$$\vec{H}^{an}_{\text{uni}} = (2K_u/M_{\text{S}})(\hat{m} \cdot \hat{e}_u)\hat{e}_u \tag{2.12}$$

For a thin film surface anisotropy can play an important role. It is described as a perpendicular uniaxial anisotropy along $\hat{e}_\perp$:

$$\begin{aligned} \mathcal{E}^{an}_{\text{surf}} &= -\frac{K_\perp}{d}(\hat{e}_\perp \cdot \hat{m})^2, \\ \vec{H}^{an}_{\text{surf}} &= \frac{2K_\perp}{\mu_0 d M_{\text{S}}}(\hat{e}_\perp \cdot \hat{m})^2 \hat{e}_\perp. \end{aligned} \tag{2.13}$$

The thickness of the material is d.

Zeeman interaction

Zeeman interaction is the interaction between an external field $\vec{H}_{\text{ext}}$ and a magnetic system. The system will respond in order to minimize energy, therefore the energy contribution is:

$$\mathcal{E}_{\text{Z}} = -\frac{\mu_0}{V}\int_V (\vec{H}_{\text{ext}} \cdot \vec{M})dV \tag{2.14}$$

Summing up interactions

Total energy functional is built by summation of energy densities due to interactions featuring the studied system (Eq. 2.15):

$$\mathcal{E}_{\text{TOT}} = \mathcal{E}_{\text{ex}} + \mathcal{E}_{\text{D}} + \mathcal{E}^{an}_{\text{uni}} + \mathcal{E}^{\text{an}}_{\text{surf}} + \mathcal{E}_{\text{Z}} \tag{2.15}$$

To find the effective field we can use the total energy per volume unit:

$$\vec{H}_{\text{eff}} = -\frac{1}{\mu_0}\, \vec{\nabla}_{\vec{M}} \mathcal{E}_{\text{TOT}} \tag{2.16}$$

2.2 Magnetization dynamics

For dynamic processes a continuum approach will be adopted as it has been done for computing energy terms in the static case.

2.2.1 Equation of motion

Precessional motion

Following the detailed analysis developed in [Gur00] let us consider a ferromagnet made of classical tops with angular momentum $\vec{J}$ and magnetic moment $\vec{\mathcal{M}}$. Considering the total magnetic field $\vec{H}$ the equation of motion reads:

$$\hbar \frac{d\vec{J}}{dt} = \vec{\mathcal{M}} \times \vec{H} \tag{2.17}$$

Let us now take into account a volume unit with N tops and consider the quantum mechanical relations:

$$\begin{aligned} \hat{\vec{\mathcal{M}}} &= -\hbar\gamma\hat{\vec{J}} \\ \text{with} \qquad \gamma &= \frac{\mu_B g}{\hbar} \end{aligned} \tag{2.18}$$

where μ_B is the Bohr magneton and g is the Lande factor. Then eq 2.17 can be transformed into:

$$\frac{d\vec{M}}{dt} = -\gamma\vec{M} \times \vec{H} \tag{2.19}$$

This approach holds for uniform magnetization and is a good approximation for slowly spatially varying magnetization. Eq 2.19 does not include damping and it conserves $|\vec{M}|$ in time. Having fixed the intensity of the magnetization upon system evolution $\vec{M}$ will change following a trajectory on the surface of a sphere with radius $|\vec{M}|$; this motion is called *precession*.

Magnetic losses

The *Landau-Lifshitz equation* (LLE) with damping reads [Lan00]:

$$\frac{d\vec{M}}{dt} = -\gamma\vec{M} \times \vec{H} - \frac{\gamma\lambda}{|\vec{M}|^2}[\vec{M} \times (\vec{M} \times \vec{H})] \tag{2.20}$$

The dissipation parameter λ has the dimension of a magnetic field. Gilbert proposed the following modification to LLE (*Landau-Lifshitz-Gilbert equation*, LLGE):

$$\frac{d\vec{M}}{dt} = -\gamma\vec{M} \times \vec{H} + \frac{\alpha}{|\vec{M}|}\left(\vec{M} \times \frac{d\vec{M}}{dt}\right) \tag{2.21}$$

He modeled damping as a viscous force. Here magnetic losses are proportional to the rate of change of $\vec{M}$. LLE transforms in LLG applying these substitutions:

$$\begin{aligned} \gamma &\rightarrow \frac{\gamma}{1+\alpha^2} \\ \lambda &\rightarrow \frac{\alpha|\vec{M}|}{1+\alpha^2} \end{aligned} \tag{2.22}$$

Both LLE and LLGE equations conserve the magnetization modulus $|\vec{M}|$.

According to a thermodynamic approach the equilibrium configuration is found by Gibbs free energy minimmzation. The minimization problem has a constraint given by the fixed magnetization length. Therefore the equation that expresses static condition reads [Sta00], [Gur00]:

$$\vec{M} \times \vec{\nabla}_{\vec{M}} \mathcal{E}_{\text{TOT}} = 0 \tag{2.23}$$

Torque on the system is zero at the equilibrium. Eq. 2.21 is generalized by the replacement $\vec{H} \to \vec{H}_{\text{eff}}$:

$$\frac{d\vec{M}}{dt} = -\gamma \vec{M} \times \vec{H}_{\text{eff}} + \frac{\alpha}{|\vec{M}|} \left(\vec{M} \times \frac{d\vec{M}}{dt} \right) \tag{2.24}$$

2.2.2 Linearized equation of motion

To model high-frequency magnetic response of a material let us consider

$$\begin{aligned} \vec{M} &= \vec{M}_0 + \vec{m}_\sim \\ \vec{H} &= \vec{H}_0 + \vec{h}_\sim \end{aligned} \tag{2.25}$$

with the dynamic components (pedix $_\sim$) being significantly smaller than the corresponding static part. The equilibrium conditions reads $\vec{M}_0 \times \vec{H}_0 = 0$. At quilibrium magnetic moments are fully aligned along $\hat{z}$. Magnetization dynamics occurs on the plane transverse to $\hat{z}$: $\vec{m}_\sim = (m_x, m_y, 0)$. Let us imagine thin film condition thus neglecting in plane demagnetization factors. Because $\vec{M}_0$ is a static component $\frac{d\vec{M}}{dt} = \frac{d\vec{m}_\sim}{dt}$. Plugging Eq. 2.25 into Eq. 2.21 yields:

$$\frac{d\vec{m}_\sim}{dt} = -\gamma(\vec{M}_0 \times \vec{h}_\sim + \vec{H}_0 \times \vec{m}_\sim) + \frac{\alpha}{|\vec{M}_0|} \left(\vec{M}_0 \times \frac{d\vec{m}_\sim}{dt} \right) \tag{2.26}$$

Complex variables to model harmonic oscillations $\vec{m}_\sim e^{j\omega t}$ can be used and therefore Eq. 2.26 transforms into (j indicates the imaginary unit):

$$j\omega \vec{m}_\sim = -\gamma(\vec{M}_0 \times \vec{h}_\sim + \vec{H}_0 \times \vec{m}_\sim) + \frac{j\omega\alpha}{|\vec{M}_0|} \left(\vec{M}_0 \times \vec{m}_\sim \right) \tag{2.27}$$

2.2.3 Polder's susceptibility tensor

To explain ferromagnetic resonance (FMR) solutions to Eq. 2.27 will be worked out for both cases: (i) $\alpha = 0$ and (ii) $\alpha \neq 0$.The strategy to find solutions has been first introduced by Polder in [Pol00]. This approach will be firstly applied to solve (i) and then it will be extended for case (ii).

Motion without damping

Motion without damping is represented by$\alpha = 0$. $\vec{H}_0$ and $\vec{M}_0$ are directed along $\hat{z}$. Therefore dynamics develops in the xy plane:

$$\begin{aligned} j\omega m_x &= -\gamma(m_y H_0 - M_0 h_y), \\ j\omega m_y &= -\gamma(-m_x H_0 + M_0 h_x), \\ j\omega m_z &= 0. \end{aligned} \tag{2.28}$$

Solving for m_x and m_y one finds:

$$m_x = \chi h_x + j\chi_a h_y, \qquad m_y = -j\chi_a h_x + \chi_a h_y, \qquad m_z = 0. \tag{2.29}$$

where:

$$\chi = \frac{\omega_\mathrm{M}\omega_\mathrm{H}}{\omega_\mathrm{H}^2 - \omega^2}, \qquad \chi_a = \frac{\omega_\mathrm{M}\omega}{\omega_\mathrm{H}^2 - \omega^2}. \tag{2.30}$$

With $\omega_\mathrm{H} = \gamma H_0$ and $\omega_\mathrm{M} = \gamma M_0$. The susceptibility tensor can be expressed in a more compact fashion:

$$\overleftrightarrow{\chi} = \begin{vmatrix} \chi & j\chi_a & 0 \\ -j\chi_a & \chi & 0 \\ 0 & 0 & 0 \end{vmatrix} \tag{2.31}$$

Special features of susceptibility tensor can be highlighted.

1. h_z does not produce any AC magnetization components. Only AC transverse magnetic field induces magnetization dynamics. h_x (h_y) generates oscillations along $\hat{x}$ ($\hat{y}$) and an oscillating component along $\hat{y}$ ($\hat{x}$) with phase shift $\Delta\phi = \pi/2$. This is due to nonsymmetry of the susceptibility tensor. Such property is known as *gyrotropy*.
2. When ω equals ω_H the condition of *ferromagnetic resonance* is met [Gur00].
3. Resonant behavior in ferromagnets is only caused by circular oscillating magnetic field with right-hand rotation (with respect to $\vec{M}$) [Gur00].

Motion with damping

To obtain an expression for susceptibility tensor in case of magnetic losses ($\alpha \neq 0$) we can apply the following replacement (with j being the imaginary unit) [Gur00]:

$$\omega_\mathrm{H} \to \omega_\mathrm{H} + j\alpha\omega \tag{2.32}$$

This substitution transforms Eq. 2.19 into Eq. 2.21 assuming equilibrium condition at zeroth order holds still true: $\vec{M}_0 \times \vec{H}_0 = 0$. We are therefore motivated to directly apply Eq. 2.32 to Eq. 2.30. This creates additional complex susceptibility components $\chi \to \chi' + j\chi''$ and $\chi_a \to \chi'_a + j\chi''_a$. Expressions for these parameteres are given in [Gur00].

Resonance condition is changed according to:

$$\omega_{res} = \omega_\mathrm{H} \to \omega_{res} = \frac{\omega_\mathrm{H}}{1+\alpha^2} \tag{2.33}$$

Within a regime very close to resonance condition normalized susceptibility components can be approximated as follows:

$$\frac{\chi'}{\chi''_{res}} \approx \frac{\chi'_a}{\chi''_{a,res}} \approx \frac{\bar{\omega}}{1+\bar{\omega}^2}; \quad \frac{\chi''}{\chi''_{res}} \approx \frac{\chi''_a}{\chi''_{a,res}} \approx \frac{1}{1+\bar{\omega}^2} \qquad \text{with} \quad \bar{\omega} = \frac{\omega - \omega_\mathrm{H}}{\alpha\omega_\mathrm{H}} \tag{2.34}$$

According to this model the resonance peak has lorentzian shape. The full width at half maximum (FWHM) is $\Delta\omega = 2\alpha\omega$. The ferromagnetic resonance depends on the shape of the sampl [Kit00].

2.2.4 Relaxation processes

We have introduced the Gilbert damping parameter α which led to the formulation of the LLG equation (Eq. 2.24). The parameter α phenomenologically models the total contribution of different kinds of relaxation processes in a magnetic system. We provide a short overview of relevant mechanisms for magnetization damping.

Energy can be dissipated by (i) coupling of different magnetic modes, *spin-spin relaxation* and (ii) by coupling to non magnetic mode system, i.e. charge carriers and lattice, *spin-lattice relaxation*. In (i) relaxation is mediated by defects and/or impurities, in case of nearly ideal crystals coupling between initially excited mode by the external field and other eigenmodes can occur directly. In (ii) spin-lattice relaxation can occur indirectly, energy is transferred to the lattice after other relaxation mechanisms, or directly, in this case the process involves direct annihilation/creation of magnons/phonons [Gur00].

For metallic magnetic materials two damping mechanisms are important for magnetization dynamics: scattering with itinerant electrons and eddy currents [Gur00], [Bil00]. [Hei00], [Ben00]. Since we study insulating magnetic materials these two mechanisms are not described further.

Two-magnon scattering (TMS)

This is a spin-spin relaxation process that occurs for non-ideal crystals. The relaxation is mediated by nonuniformities. The relevant nonuniformities are [Gur00]: (i) heterogeneity in chemical composition, e.g. partial disorder in ions organization within the lattice; (ii) variation of crystal axes, e.g. polycrystalline materials; (iii) dislocations causing spatially varying stress in the sample; (iv) surface roughness and surface or interface defects [Ari00]. In TMS energy is transferred from the uniform eigenmode to other eigenmodes having non-zero wave vector and being degenerate with the FMR response. Coupling of these modes occurs via dipolar interaction with the scatterer (the nonuniformity), for this reason the coupling is $\vec{k}$-dependent, i.e. coupling strength depends in spi nwave propagation direction [Hur00]. TMS is an extrinsic term in linewidth total contribution. It is non-Gilbert like damping i.e. not proportional to resonance frequency in field linewidth [Lin00]. When TMS gives important contribution to resonance peak broadening the magnetization dynamics is better described by Bloch-Bloembergen equation which applies when magnetization length is not conserved [Bloe00], [Gur00], [Bil00]. In TMS energy is firstly transferred from uniform precession to degenerate magnons with $\vec{k} \neq 0$ and finally energy is transferred to the lattice which results in heating.

Multimagnon scattering

Inherent spin-spin processes can involve more than two magnons. Probability for these processes to occur decreases with higher number of magnons partecipating in it. Energy and wave vector are conserved in these relaxation mechanisms without the need for nonuniformity.

For three magnon processes two mechanisms can occur: splitting and confluence. Three magnon processes are usually controlled by dipole-dipole interaction whereas four magnon scattering can be caused by exchange interaction. These scattering processes are generally described by kinetic equation which defines a characteristic relaxation time $\frac{1}{2\omega_r}$. Linear relaxation theory allows to write the kinetic equation as: $\frac{dn}{dt} = -2\omega_r(n - \bar{n})$, with n being the off-equilibrium magnon population and $\bar{n}$ being the equilibrium population of magnons with energy ϵ_n and wave vector $\vec{n}$. ω_r depends on temperature and on interactions that determine the scattering process. For a detailed explanation the reader may consult [Gur00]

Spin pumping

It has been investigated that a spin current exerts a torque on the magnetic order of a material and viceversa a precessing magnetization of a system can transfer angular momentum to adjacent layers thus acting as a spin pump [Tse00]. The concept of 'mixing conductance' ($g^{\uparrow\downarrow}$) is used to model spin pumping [Bra00]. Spin pumping causes a variation of both γ and α. This process contributes to linewidth broadening as a Gilbert-like term. The spin current that is pumped by the precessing magnetization is determined by the spin mixing conductance: $I_S^{pump} \propto g^{\uparrow\downarrow}\left(\hat{m} \times \frac{d\hat{m}}{dt}\right)$, with $\hat{m}$ being the magnetization unit vector [Bra01]. The additional term to the damping constant can be expressed as follows [Ger00]: $\alpha' = g^{\uparrow\downarrow}\frac{\gamma h}{AM_{\mathrm{S}}d}$; with h being the Planck's constant, d the thickness of the magnetic layer and A the interface area. In case spin pumping effect can not be be neglected the damping constant transforms as follows: $\alpha \rightarrow \alpha + \alpha'$. The effect of spin pumping is typical for high atomic number Z materials with large spin-orbit coupling. The pumped spin current undergoes spin flip scattering. Spin flip relaxation rate (τ_{SF}^{-1}) depends on Z as follows: $\tau_{\mathrm{SF}}^{-1} \propto Z^4$ [Tse00].

The interested reader may refer for details to [Kap00], [Car00], [Bra02].

2.2.5 Eigenoscillations of an ellipsoid

In deriving Polder's susceptibility we did not take into account the spatial variation within the sample of magnetic field and magnetization and how these two interact. Spatial distribution of magnetic field and magnetization are found by solving Maxwell's equation with proper boundary conditions.

A small magnetic ellipsoid interacting with an external field is here studied. By *small* it is meant the the size of the sample is smaller than the electromagnetic wave in medium itself. The *external* field $\vec{H}$ is uniform by hypothesis. Then the internal field, considering demagnetization, reads:

$$\vec{H}_i = \vec{H} - \overleftrightarrow{N} \cdot \vec{M} = \vec{H} - \vec{H}_{\mathrm{D}} \tag{2.35}$$

The demagnetization tensor is symmetric and can be diagonalized by assuming as reference system the axes of the ellipsoid. Then the trace of $\overleftrightarrow{N}$ satisfies $N_x + N_y + N_z = 1$. The linearized equation of motion transforms in:

$$j\omega\vec{m}_\sim = -\gamma[\vec{M}_0 \times (\vec{h}_\sim - \overleftrightarrow{N}\vec{m}_\sim) + (\vec{H} - \overleftrightarrow{N}\vec{M}) \times \vec{m}_\sim)] + \frac{j\omega\alpha}{|\vec{M}_0|}\left(\vec{M}_0 \times \vec{m}_\sim\right) \tag{2.36}$$

Upon the replacements $\vec{H} \rightarrow \vec{H} - \overleftrightarrow{N} \cdot \vec{M}$ and $\vec{h}_\sim \rightarrow \vec{h}_\sim - \overleftrightarrow{N} \cdot \vec{m}_\sim$ in Eq. 2.21.

To investigate resonant modes of the system we suppose zero dynamic external field and zero damping. For $\vec{H}$ collinear with one of the ellipsoid axes and along $\hat{z}$, $\overleftrightarrow{N}$ is diagonalized. Then Kittel's formula is valid [Kit00]:

$$\omega_0 = \gamma\sqrt{[H(N_x - N_z)M_0][H - (N_y - N_z)M_0]} \tag{2.37}$$

In this case $\hat{z}$ is aligned with one of the ellipsoid axis. $\vec{M}_0$ is also along $\hat{z}$.

2.3 Ferromagnetic resonance for anisotropic materials

2.3.1 Effective demagnetization tensor

To analyze FMR for anisotropic materials two methods can be used: (effective demagnetization factors or (ii) the spherical coordinates method [Gur00]. We should focus on (i). Here we shortly comment on (i). The effective field is written as:

$$\vec{H}_{\text{eff}} = \overleftrightarrow{N}_{\text{eff}} \vec{M}. \tag{2.38}$$

$\overleftrightarrow{N}_{\text{eff}}$ is the effective demagnetization tensor. This allows to take into account anisotropy field. In this picture to the conventional demagnetization parameters other terms are added that depend on the kind of anistropy and on the relevant angles of the system, i.e. the angle between magnetization and anisotropy axis and the angle between the applied field and the anisotorpy axis. For the case of a plane sample magnetized along $\hat{z}$ with uniaxial anisotropy the additional terms that modifies Eq. 2.37 are:

$$\begin{aligned} N_x^{an} &= \frac{2K_u}{M_z^2} \\ N_y^{an} &= \frac{2K_u}{M_z^2} \end{aligned} \tag{2.39}$$

For small magnetization oscillations we could assume $M_{\text{S}} \approx M_z$. Using this formalism for Kittel's formula reduces to [Kit00]:

$$\omega = \gamma\mu_0 \sqrt{\left[\left(H + \frac{2K_u}{M_{\text{S}}}\right)\left(H + \frac{2K_u}{M_{\text{S}}} + M_{\text{S}}\right)\right]} \tag{2.40}$$

For a detailed analysis on different types of anisotropy the reader may consult [Gur00].

2.3.2 Polycrystalline materials

Let us assume that a polycrystalline material can be modelled according to independent grain approximation, i.e. influence of shape of the grains and coupling between grains can be both neglected. We are interested in the case of $H_A \gg M_{\text{S}}$, i.e. the anisotropy field is larger than the typical magnetization of the sample. Calculating the susceptibility tensor is a challenging task for this type of magnetic systems. Schlömann was the first to investigate this problem for different type crystal structure [Sch01], [Sch02]. He described the magnetic resonance in terms of resonant field by introducing the distribution of resonant field strength $w(H)$ as a function of η and ρ which are the angle that define the direction of the applied static field (H_{ext}) in the reference system of the crystal structure (see Eq.2.41)

$$w(H_{\text{ext}}) = \frac{1}{4\pi} \int_{sphere} d\Omega \, \delta[H_{\text{ext}} - H_{res}(\omega, \eta, \rho)] \tag{2.41}$$

With $d\Omega$ being the infinitesimal part of the solid angle. Eq. 2.41 is used to then compute the susceptibility tensor components assuming uniform grain distribution [Sch01]. Allowing for a finite single crystal linewidth the singularities of $w(H_{\text{ext}})$ the resonance spectrum of a polycrystalline in independent grain approximation and for large anisotropy can exhibit two maxima [Gur00], [Sch01], [Sch02]. The linewidth of a polycrystal can be approximated to be [Gur00]:

$$(\Delta H)_{an} \sim \frac{2K_1}{M_{\mathrm{S}}} \tag{2.42}$$

With K_1 being the first-order anisotropy constant. The maximum shift of resonance curve is estimated to be [Gur00]:

$$(\delta H)_{an} \sim \frac{K_1}{2M_{\mathrm{S}}} \tag{2.43}$$

For a detailed description of FMR in polycrystalline materials the reader may consult [Gur00], [Zhu00], [Kal00], [Sch00].

2.4 Spin waves

So far uniform magnetization motion has been treated. Spins are uniformly perturbed, they precess with the same phase. These wave-like excitations are described by an infinite wavelength hence zero wavevector. Starting from magnetostatic modes (*Walker's modes* [Wal00]) we then introduce wave-like excitations of the magnetic order with non zero wavevector $\vec{k}$. Propagating perturbations of the magnetic order of a materials are called spin waves or magnons. Existing models to describe spin waves dominated by dipolar interaction are commented. We conclude by presenting a model that describes spin waves in thin films in mixed dipole-exchange regime [Kali00]. The description that we will give follows the approach of [Sta00] and [Wal00].

2.4.1 Walker's modes

Quasi-static approximation to Maxwell's equation reads:

$$\begin{aligned} \vec{\nabla} \times \vec{H} &= 0, \\ \vec{\nabla} \cdot \vec{B} &= 0, \\ \vec{\nabla} \times \vec{E} &= j\omega\vec{B}, \\ \text{with} \quad \vec{B} &= \vec{\mu}\vec{H} \end{aligned} \tag{2.44}$$

$\vec{h}$ can be written as gradient of a scalar function that is called magnetostatic potential as already discussed in 2.1.2. Then it holds:

$$\vec{\nabla}(\vec{\mu} \cdot \vec{\nabla}\psi) = 0 \tag{2.45}$$

This is called Walker's equation and is used in quasistatic magnetism. Let us now deal with a ferrite magnetized along $\hat{z}$ and neglect anisotropy and exchange contribution. here the ferrite is assumed to be infinitely large. Propagation angle wih respect to $\hat{z}$ is θ. The resonance condition reads:

$$\omega = \sqrt{\omega_{\mathrm{H}}(\omega_{\mathrm{H}} + \omega_{\mathrm{M}} sin^2\theta)} \tag{2.46}$$

This result does not depend on the wavelength. This degeneracy is removed when exchange interaction and the finiteness of the system are considered.

To account for exchange interaction the following replacement is applied: $\omega_\mathrm{H} \rightarrow \omega_\mathrm{H} + \lambda_{ex}^2 k^2 \omega_\mathrm{M}$. Eq. 2.46 changes accordingly:

$$\omega = \sqrt{(\omega_\mathrm{H} + \lambda_{ex}^2 k^2 \omega_\mathrm{M})[\omega_\mathrm{H} + \omega_\mathrm{M}(\lambda_{ex}^2 k^2 + sin^2\theta)]} \tag{2.47}$$

We can conclude that for $\lambda_{ex}^2 k^2 \ll 1$ wave-like excitations of magnetization are dominated by dipole-dipole interaction and they are referred to as either dipolar spin waves or magnetostatic modes; whereas for $\lambda_{ex}^2 k^2 \gg 1$ magnetization dynamics is ruled by quantum mechanical exchange interaction.

2.4.2 Dipolar regime

In this section a short explanation of different excitation geometries in dipolar regime is provided according to the approach of [Sta00]. According to the angle between equilibrium magnetization and spin wave propagation, spin waves display different properties.

Exchange and anisotropy are neglected. Magnetic system is imagined to be a thin film. d is the film thickness.

Magnetostatic forward volume waves - MSFVW

Magnetization ($\vec{M}$) is out of plane and spin wave propagation is in plane ($\vec{M} \perp \vec{K}_{inp}$, with $\vec{k}_{inp}$ being the spin wave vector).

This is a uniformly distributed volume mode. Mode amplitude is periodic along the thickness axis. Therefore all modes display same cutoff frequency. Dispersion relation does not depend on the direction of the in-plane wavevector but only on its magnitude, therefore the dispersion relation is isotropic. The term *forward* relates to the characteristic that phase and group velocity have same positive direction. To include anistropy let us redefine ω_M as $\omega_\mathrm{M} \rightarrow \omega_\mathrm{eff} = \gamma(M_\mathrm{S} - \frac{2K}{d\mu_0 M_s})$. The dispersion relation for MSFVW is [Sta00]:

$$\omega_\mathrm{MSFVW} = \left\{\omega_\mathrm{H}\left[\omega_\mathrm{H} + \omega_\mathrm{eff}\left(1 - \frac{1 - e^{-k_\mathrm{inp}d}}{k_\mathrm{inp}d}\right)\right]\right\}^{1/2}. \tag{2.48}$$

Magnetostatic surface waves - MSSW

Magnetization and spin wave propagation are both in plane and perpendicular to each other ($\vec{M} \perp \vec{k}_{inp}$). These are surface localized wave. The first scientists to study this magnon propagation were Damon and Eshbach [Dam00]. These MSSWs are often referred to as Damon-Eshbach spin waves. Because of the asymmetry of the spatial profile of the dipolar field Damon-Eshbach spin waves are nonreciprocal [Gla00]. Phase and group velocity point in same positive direction therefore MSSWs are forward waves. Mode amplitude decays exponentially from surface towards bulk.

The dispersion relation in this configuration is [Sta00]:

$$\omega_\mathrm{MSSW} = \left[\omega_\mathrm{H}(\omega_\mathrm{H} + \omega_\mathrm{eff}) + \left(\frac{\omega_\mathrm{eff}}{2}\right)^2 \cdot \left(1 - e^{-2k_\mathrm{inp}d}\right)\right]^{1/2}. \tag{2.49}$$

The amplitude of oscillation for non reciprocal propagation has been calculated by Demokritov et al. [Dem01]:

$$m_\pm^n \propto \left[\frac{f_n}{\gamma} \pm \frac{1}{M_\mathrm{S}}\left(H_\mathrm{ext}^2 - \frac{f_n^2}{\gamma^2}\right)\right] \tag{2.50}$$

With f_n being the resonance frequency of the n^{th} mode and H_{ext} the static external applied field. Eq. 2.50 does not consider anisotropy, therefore M_{eff} is replaced by M_{S}.

Magnetostatic backward volume waves - MSBVW

Now assume that the magnetization is in plane and parallel to spin wave propagation direction ($\vec{M} \parallel \vec{k}_{inp}$). Mode amplitude is distributed uniformly across the thickness. The dispersion relation is given by [Sta00]:

$$\omega_{\text{MSBVW}} = \left\{ \omega_{\text{H}} \left[\omega_{\text{H}} + \omega_{\text{eff}} \left(\frac{1 - e^{-k_{\text{inp}} d}}{k_{\text{inp}} d} \right) \right] \right\}^{1/2}. \tag{2.51}$$

This mode is called magnetostatic backward volume. Group velocity has negative sign, i.e. frequency decreases for higher resonant modes.

2.4.3 Dipole-Exchange regime

In the previous section the dipolar regime of spin wave excitation has been described according to both magnetization and SW propagation direction. We should analyze the nature of spin wave when both dipolar and exchange interactions are considered.

Kalinikos-Slavin formalism for a thin film

The model assumes that: (i) sample thickness is significantly smaller than other two dimensions and (ii) film is isotropic therefore crystalline anisotropy is neglected. Kalinikos Slavin theory sets out to express the frequency spectrum $\omega(\vec{k}_{inp})$. This study considers magnetic dipolar interaction, non-uniform exchange interaction and mixed surface spin pinning boundary conditions [Kali00]. Assuming magnetization vector is uniform at boundaries despite the spin pinning the equation to calculate the resonant frequency is given by:

$$\omega_n = [(\omega_{\text{H}} + \lambda_{ex}^2 \omega_{\text{M}} k_n^2)(\omega_{\text{H}} + \lambda_{ex}^2 \omega_{\text{M}} k_n^2 + \omega_{\text{M}} F_{nn})]^{1/2}. \tag{2.52}$$

F_{nn} is the parameter that describes dipolar interactions and depends on P_{nn} which can be epxressed as a function of kd. The total wave vector is found by $k_n^2 = k_{\text{inp}}^2 + \kappa_n^2$. k_{inp} is in plane wave vector, κ_n is quantized transverse wave vector, i.e. across the thickness. P_{nn} has different expression according to pinning condition. We shall here report the case of totally unpinned boundary ($\kappa_n = n\pi/d$, with $n = 0, 1, 2, 3, ...$) as it is the most frequently used for data fitting in this thesis:

$$\begin{aligned} P_{nm} = \left(\frac{k_{\text{inp}}}{k_m}\right)^2 \delta_{nm} + \left(\frac{k_{\text{inp}}^2}{k_n k_m}\right)^2 \frac{F_n}{\sqrt{(1+\delta_{0n})(1+\delta_{0m})}} \frac{1 + (-1^{n+m})}{2}, \\ \text{with} \quad F_n = \frac{2}{k_{\text{inp}} L}[1 - (-1)^n e^{-k_{\text{inp}} L}] \end{aligned} \tag{2.53}$$

δ_{pq} is the Kronecker delta function, n and $m = 0, 1, 2, ...$ Knowing P_{nn} we can calculate F_{nn} as:

$$F_{nn} = P_{nn} + sin^2\theta \left[1 - P_{nn}(1 + cos^2\phi) + \omega_{\text{M}} \frac{P_{nn}(1 - P_{nn}) sin^2\phi}{\omega_{\text{H}} + \lambda_{ex}^2 \omega_{\text{M}} k_n^2} \right] \tag{2.54}$$

The two angles (i) θ and (ii) ϕ are (i) the angle between thickness axis and magnetization and (ii) the angle between magnetization and propagation direction, respectively (Fig. 2.1).

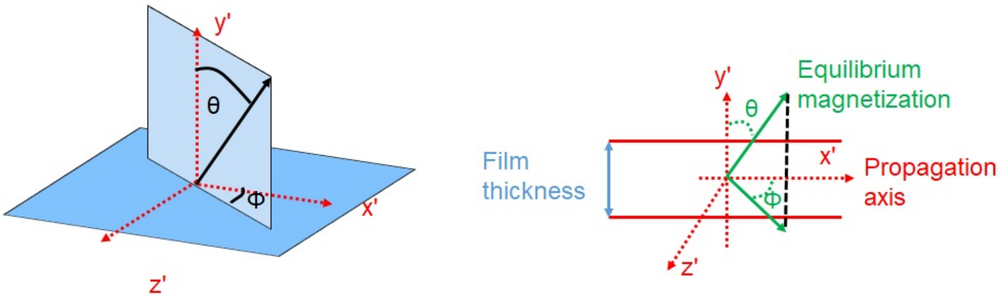

Figure 2.1: θ and ϕ are defined. These angles define the direction of the SW propagation in the magnetic thin film with respect to equilibrium magnetization and thickness axis.

It should be noted that standing spin waves can originate [Tan00] which causes spin wave resonance.

Formation of standing spin waves depends on the finite thickness of the sample, on the boundary condition and exchange interaction. Such a spin wave resonance is named *perpendicular standing spin wave* (*PSSW*).

Quantization along thickness dimension of the thin film is modelled by the discrete transverse wave number (see above):

$$\kappa_n = \frac{n\pi}{d} \tag{2.55}$$

The theoretical formalism for exchange standing spin waves can be found in [Gur00], [Sta00], [Kos00], [DeW00]. To obtain the formula for the PSSW resonant frequency the equation of motion for magnetization dynamics is modified to account for anisotropy and exchange interaction; to solve it one can use again linearization method. Equation of motion have to be combined with Maxwell's equation. Solutions need to satisfy new boundary condition that are introduced to model exchange interaction that requires continuity of the derivatives of $\vec{m}$.

To conclude this section we provide a formula to describe PSSW resonances [Mru01]:

$$\omega_n^{\mathrm{PSSW}} = \sqrt{\left[\omega_{\mathrm{H}} + \frac{2A}{M_{\mathrm{S}}}\left(\frac{n\pi}{d}\right)^2\right]\left[\omega_{\mathrm{M}} + \omega_{\mathrm{H}} + \frac{2A}{M_{\mathrm{S}}}\left(\frac{n\pi}{d}\right)^2\right]} \tag{2.56}$$

Quantization number n takes as a lowest value 1.

2.5 The grating coupler

The theory that has been discussed so far provides the basics to understand ferromagnetic resonance and spin waves.

This chapter will focus on the grating coupler which relates to a broad research within nanotechnology, e.g. photonics and plasmonics.

Indeed magnonics has recently re-adapted this concept from photonics [Eur00] and plasmonics [Rop00] to tackle one of the key challenges in the field, i.e.

microwave-to-spin wave coupling [Yu02]. This chapter is set on purpose between the discussion on general concepts of magnetism and a brief overview of resonance behavior in magnetic nanoparticles. The usage of magnetic nanoparticles that we intent to explore find scientific motivation from the magnonic grating coupler effect (section 2.5.2).

2.5.1 The grating coupler in state-of-the-art nanotechnology

In *photonics* the grating coupler is used as a technological solution to transmit light from a fiber to a planar waveguide (and viceversa). The electromagnetic coupling is challenging because of size mismatch between fiber (diameter $\gtrsim 100\,\mu$m) and thin-film planar waveguide (dimensions $\sim 1\,\mu$m).

A periodic structure is patterned at the end of the waveguide in dielectric material. The structure features periodic grooves. As light impinges it diffracts from the periodic lattice of grooves thus constructively interfering towards a specific direction. This phenomenon works (i) to couple light into the waveguide from a single mode fiber and (ii) to couple light from the waveguide into the fiber. Grating performance depends on complex propagation constant which is generally function of light polarization, structure geometry and operating frequency. A detailed analysis of optical grating couplers is provided in [Fes00].

In *plasmonics* coupling the free space light to surface plasmon polaritons (SPPs) on a flat metallic surface is a challenge [Ebb00], [Koe00]. SPPs are guided electromagnetic waves at a metal/dielectric interface. The wavelength is smaller compared to light in free space. At the same time SPPs are evanescent waves and for these reasons coupling to/from free space light is highly difficult. To improve coupling of the SPPs to light several methods have been engineered. The grating coupler is used as an element to ensure wave vector (momentum) match. The periodic groove structure has to be designed in order to provide with the correct Fourier spectrum for SPP wave-vector matching.

2.5.2 The grating coupler in magnonics

This section briefly summarizes the scientific work that implemented for the first time the concept of grating coupler on a magnonic device [Yu02] discovering the *magnonic grating coupler effect* (MGC).

The basic structure consisted of two integrated coplanar waveguides, acting as microwave antennas, on a ferro- or ferrimagnetic layer. For the grating coupler effect periodically arranged nanomagnets between the antennas and the magnetic layer were prepared (Fig. 2.2).

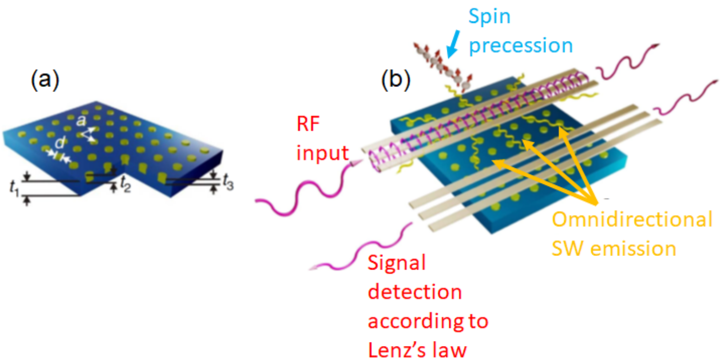

Figure 2.2: Pictures extracted from [Yu02]. (a) Representation of the 2D periodic lattice. The blue material is the magnetic layer and the green objects are the nanomagnets that are periodically arranged. d is the size of the nanomagnet and a indicates the cell vector of the lattice. t_1 is the thickness of the magnetic layer, t_2 is the total thickness of the nanomagnet and t_3 is the nanomagnet thickess in the patterned magnetic layer. (b) Blue material is magnetic layer and green material is the periodic lattice of nanomagnets. RF signal is injected in one microwave antenna. Microwave field perturbs equilibrium magnetization and spin waves are generated. Spin precessional motion can reach second antenna. Here an electrical signal is measured according to Lenz's law of induction. Because of grating coupler effect spin waves (SWs) emission is omnidirectional.

Additional spin wave resonances were found and attributed to the so-called magnonic grating coupler (MGC) effect. The Fourier spectrum of the nanomagnet array provided additional wavevectors for magnon excitation. Moreover the signal strength of grating coupler induced spin precessional motion was significantly enhanced. The two dimensional grating coupler allowed for emission along different high-symmetry directions. The MGC effect led to (i) short-waved magnon excitation and (ii) omnidirectional emission.

Grating coupler effect in magnonics was attributed to both spatially modulated magnetic susceptibility and stray field effects. The periodic modulation provided additional Fourier components representing reciprocal lattice vectors $\vec{G}$. Both antennas (emitter and receiver)were fabricated on top of the periodic arrays of nanomagnets. The interaction of the periodic lattice with magnons leads to grating coupler induced modes.

In addition to the dependence on material properties (e.g. susceptibility) the magnonic grating coupler effect depends on lattice constant of the nanomagnet array and on its filling factor. The geometrical parameters, lattice constant and filling factor, are important for RF field enhancement as it can be explained by the formalism in [Au00].

Reducing the diameter of the nanomagnet is expected to excite higher resonant modes. Signal strength increases with the filling factor. Materials optimization can further improve the application of the magnonic grating coupler. Nevertheless top down approach suffers of nanolithography limitations.

To overcome these technological limitations and push forward the potential of the grating coupler concept in magnonics magnetic nanoparticles are explored as possible magnon nanoemitters. The MGC effect paved the path for efficient coupling. This was achieved by a periodic struture spatially modulating magnetic properties of the device. From magnetic scattering fomalism [Au00] it is predicted that the stray field enhancement due to the periodic arrangement of nanomagnets is increased by decreasing the lattice constant at fixed nanomagnet's diameter. This improvement for MGC is limited in a top-down approach by nanolithography because of light diffraction limit.

Magnetic nanoparticles (NPs) are therefore investigated to overcome the limitations of nanolithography. The size of the NPs can be as small as few nm. Material choice is also important to exploit other characteristic such as magnetic anisotropy. In particular hexaferrite materials features large magnetocrystalline anisotropy. For this reason these materials have large FMR frequency ($\gtrsim$ 50 GHz) at zero applied field. This peculiarity can be exploited to extend the resonant grating coupler modes to higher frequencies.

Varying NP size allows to explore different magnetic behavior e.g. ferrimagnetic and superparamagnetic.

Following the findings in [Yu02] a so far untested method for improving microwave-to-magnon coupling is investigated in this thesis. Magnetic NPs are deposited on the surface of a ferrimagnetic layer. The effect of NP distribution of spin wave propagation properties in the ferrimagnetic layer is the subject of our research.

2.6 Magnetism of nanoparticles

This section offers a general overview of methods to describe magnetic behavior of nanoparticles. In this thesis different type of nanoparticles have been explored (hexaferrite and iron oxide based). These were neither arranged in any periodic manner nor perfectly monodispersed. As it will be shown in chapter 5 nanoparticles tend to form clusters. Clusters' sizes depend on the nanoparticle material and suspension and can range from hundreds of nm to tens of μm.

Shrinking down to the nanoscale the lateral dimensions of a system increases the importance of surface and finite-size effects. It has been estimated that a magnetic spherical particle becomes single doman if its radius fulfils [Han00]:

$$R \leq R_c = \frac{6\sqrt{AK}}{\mu_0 M_s^2} \tag{2.57}$$

With K being the relevant magnetic anisotropy constant.

Magnetic anisotropy of a nanoparticle is often modeled with an effective constant. Surface effects destabilize magnetic order at the outermost layer of the nanoparticle. Nanoparticles can be depicted as two phase systems composed of a core and a surface layer ([Pap00]) and the effective anisotropy K is found by:

$$K = K_C + \frac{6K_S}{2R} \tag{2.58}$$

K_C is the magnetocrystalline anisotropy of the core and K_S is the surface anisotropy. Anisotropy is treated as uniaxial.

The Stoner-Wohlfart (SW) model [Han00] describes coherent magnetization rotation of a single domain magnet. Being H the external field the total energy of the system (with volume V) depends on angular orientation of applied field (θ) and magnetic moment (ϕ) with respect to anisotropy axis (refer to Fig. 2.3):

$$\mathcal{E}_{SW} = KVsin^2\phi - \mu_0 HM_sVcos(\theta - \phi) \tag{2.59}$$

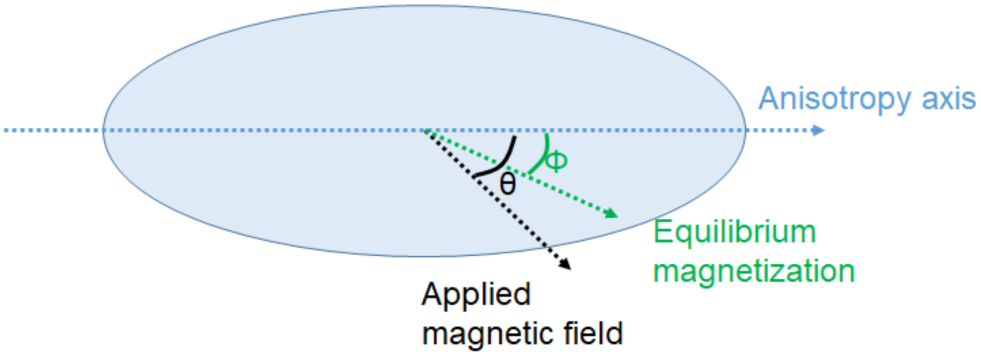

Figure 2.3: Prolate shape. Angles defines direction of magnetization and applied field with respect to anisotropy axis.

This model can be used to find the ground state magnetization $\vec{M}_S$ which will be then used to solve the linearized LLGE. Using Eq. 2.59 the equilibrium magnetization is found by energy minimization with respect to the two angular variables θ and ϕ.

The functional Eq. 2.16 is used to find the total effective field. The total effective field that rules particle magnetodynamics is written as [Shi00]:

$$\vec{H}_{\text{eff}} = \vec{H}_{\text{ext}} + \frac{2A}{\mu_0 M_s}\vec{\nabla}^2\vec{m} + H_K(\hat{e}_M \cdot \hat{e}_u)\hat{e}_u - \vec{H}_{\text{D}} \tag{2.60}$$

With H_K being the effective anisotropy field.

Ferromagnetic resonance in nanoparticles is extensively investigated for the case of ferrite based materials along with a theoretical analysis in [Shi00], [Shi01]. In [Shi00] the cases of easy axis *(i)* parallel to external field and *(ii)* perpendicular to the external are analyzed for ferrite nanoparticles with uniaxial anisotropy:

$$\begin{aligned} \omega_{\parallel} &= \gamma\left(H_{\text{ext}} + H_{uni}^{an} + \frac{6K_S}{M_s d}\right) \quad (i) \\ \omega_{\perp} &= \gamma\left[H_{\text{ext}} - \frac{1}{2}\left(H_{uni}^{an} + \frac{6K_{surf}}{M_s d}\right)\right] \quad (ii) \end{aligned} \tag{2.61}$$

3. Experimental techniques

In this chapter experimental setups and techniques are described. The employed measurement techniques are based on electrical detection (section 3.1) and optical detection (section 3.2) of magnons.

3.1 Vector Network Analyzer

In information and communication technology (ICT) vector network analysis is a reliable method to characterize device performance by measuring test signals. A signal conveying information can be divided up in amplitude and phase. These two components can be altered by the device under test (DUT) and this effect can be power- and frequency-dependent [Key00]. Microwave engineering concepts will be adopted in the following to analyze how a vector network analyzer (VNA) can stimulate magnetization oscillations and monitor spin wave propagation.

3.1.1 Scattering parameters

Scattering matrix ($\hat{S}$) and distributed model formalism are the conventional approaches to analyze circuits within radiofrequency (RF) regime. The scattering matrix is a $n \times n$ matrix where n equals the number of ports featuring the network that has to be characterized. The scattering matrix represents a set of parameters ("S-parameters") that relate to reflection and transmission of a travelling wave that is sent to the DUT [And00]. "S-parameters" measure reflected and transmitted power in relative terms. Normalized to incident power parameters do not depend on absolute power and source power variations with frequency assuming linear response [Key00]. For a 2-port network following equations relate signal amplitudes a and b with scattering parameters S_{pq} Fig. 3.1

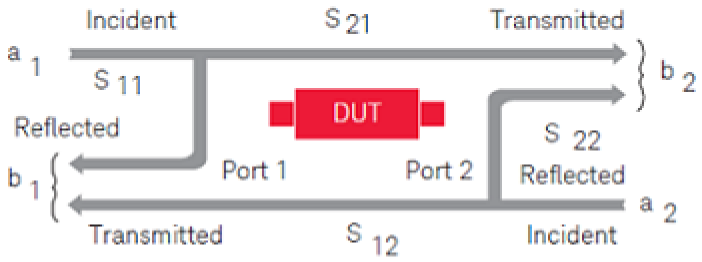

Figure 3.1: From [Key00]. The picture represents two incident signals and the effect of the DUT is either to reflect them back or to transmit them. $(S_{pq})_{pq=1,2}$ are the scattering parameters. The conventional labelling indicates with first number the receiver port and with the second number the emitting port. To give few practical examples, S_{11} measures the portion of the signal emitted from port 1 and detected at port 1 because of reflection; S_{21} measures the portion of the signal emitted from port 1 and detected at port 2. a_p and b_p, with $p = 1, 2$, are the normalized voltage waves.

$$\begin{pmatrix} b_1 \\ b_2 \end{pmatrix} = \begin{bmatrix} S_{11} & S_{12} \\ S_{21} & S_{22} \end{bmatrix} \begin{pmatrix} a_1 \\ a_2 \end{pmatrix} \tag{3.1}$$

Signal scattering depends upon connections of successive elements within the same radiofrequency circuit. Interfacing different components is crucial for information transfer and power distribution. This issue is known as impedance matching and is discussed in 3.1.2.

3.1.2 Impedance matching

Given a generic electrical source with complex impedance Z_S and a load impedance Z_L that is connected to this power generator (Fig. 3.2), it can be demonstrated that power transfer is maximum when

$$Z_L = Z_S^* \tag{3.2}$$

is fulfilled. The apex $*$ represents the complex conjugate. This situation corresponds to *matching*. Impedance mismatch along a transmission line can lead to signal backreflection, phase distortion and power loss for the signal output.

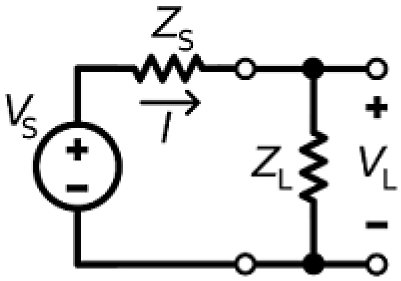

Figure 3.2: Thevenin equivalent of source circuit with load impedance. Active power flows from source impedance Z_S to load impedance Z_L where output voltage V_L is measured. For an arbitrary situation both impedances are complex hence constituted by a passive and reactive part: $Z_S = R_S + jX_S$ and $Z_S = R_L + jX_L$ with j being the imaginary unit. V_S is the source voltage.

Impedance matching is done starting from a reference source impedance. For RF circuits a reference impedance is a real positive variable without reactance e.g. $Z_S = R_S = 50\,\Omega$. Therefore to maximize signal transfer and enhance excitation of magnetization perturbation our coplanar waveguide design (CPW) design (4) needs to be optimized for $50\,\Omega$ impedance matching. This means that the geometry of the coplanar waveguide is to be conceived in such a way to determine a CPW characteristic impedance Z_0 as close as possible to $50\,\Omega$. Geometry can be tuned to obtain $Z_0 = Z_S$.

Fig. 3.3 illustrates the cross sectional view of a typical coplanar waveguide structure.

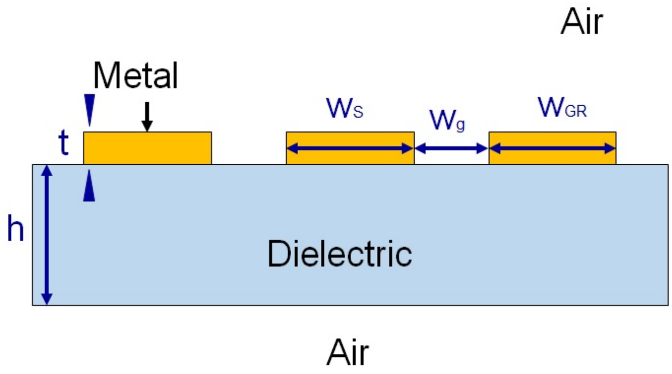

Figure 3.3: Cross sectional view of CPW structure, from [Wad00]. The parameters for the relevant CPWs used in this thesis are given in chapter 4. Substrate is a dielectric material. On top of the dielectric the CPW is fabricated (three metal lines). The surrounding environment is air. $\mathrm{W_S}$, $\mathrm{W_g}$ and $\mathrm{W_{GR}}$ are respectively signal line width, gap width between conductive strips and ground line width.

For a detailed discussionanalysis the reader may consult [Wad00], [Bil00], explain the formalism to calculate characteristic impedance as function of geometrical parameters is not essential for the purpose of this thesis work.

For signal transmission and data acquisition the calibration of the VNA is of key importance.

3.1.3 Calibration of the vector network analyzer

Calibration is essential to compensate for errors such as [Agi00]:

1. systematic errors
2. drift-induced errors
3. random errors

Systematic errors do not change in time and are caused by imperfections in analyzer and setup. Systematic error are removed after calibration. Drift causes a change in setup performance after calibration. Drift is usually due to temperature variations. Advanced calibration techniques can provide solutions for this kind of error. Random errors can not be compensated via calibration as they vary in time in a random manner. No calibration can correct random errors.

Measurement calibration is a mathematical model that compensates the effect of systematic errors. Measurements of known devices or calibration standards connected at fixed measurement plane are performed for calibration. This procedure elaborates numerical coefficients that will then be used to define a constant reference plane for zero phase shift, zero backreflection, transmission without losses and known impedance [Key01].

Different methods for calibration are available. In the course of this thesis the *SOLT* method has been adopted. SOLT stands for Short-Open-Load-Thru and these four terms relate to components of a calibration chip for microwave tips. SOLT technique consists in a full 2-port vector-error correction analysis. It measures scattering parameters in forward and reverse direction.

The interested reader may find a detailed explanation of error models and calibration techniques in [Key02].

3.1.4 Experimental setup

A vector network analyer (VNA) is combined with an integrated coplanar waveguide to create a broadband spin wave spectrometer. With this broadband spectroscopy method the magnetization dynamics of the nanoparticles decorated yttrium iron garnet is explored. We have performed all electrical spin wave spectroscopy (AESWS) which is an inductive technique based electrial on excitation and detection of magnons that relates to the commonly known VNA ferromagnetic resonance (VNA-FMR). The difference is that with the former methodology spin waves with non zero wavevector are excited whereas with the latter uniform spin precession is generated hence wavevector is zero. AESWS is also known as propagating spin wave spectroscopy (PSWS) [Mel00], [Bao00].

The measurement setup is hosted on top of a shock absorbing table to isolate the system from external vibrations. The PNA N-5222A vector network from Agilent is installed. It has 4 ports, every port can emit and receive power. Noise floor is -114 dBm and dynamic range 127 dB. The frequency range is 10 MHz $\div$ 26.5 GHz. Voltage at each port is measured at the same frequency.

Electrical contact between a port the device under test (DUT) is established with a high-frequency cable and microwaves tip. Particular care is required when installing and fixing cables and tips. A non-balanced torque causes degradation of impedance matching. RF cables are connected using a calibrated torchwrench and held steady by mechanical mounts. Microwave tips are mounted at the hosting end of the corresponding micropositiong stages.

Sample housing is at the center of the vibration-cushioned table. It is designed to fix the chip by the generation of vacuum at its base. Fixing the chip avoid moving it when probey are brought closer in mechanical contact.

The sample is symmetrically surrounded by four pole shoes forming the cores of coils. The pole shoe provide an in plane magnetic field with arbitrary orientation. The intensity of the generated DC magnetic field is $|\mu_0 H| \leq 90$ mT. The power supplies is bipolar therefore both negative and positive fields are available. In addition magnetic field can be swept during measurement or kept fixed at a specified value.

A LabView routine is used to configure the measurement from a computer. This allows to set the frequency range and power level. It also permits to configure magnetic field magnitude and orientation sweep.

3.1.5 Physical working principle

VNA-AESWS is an inductive technique which uses electrical detection for travelling spin waves Fig. 3.4.

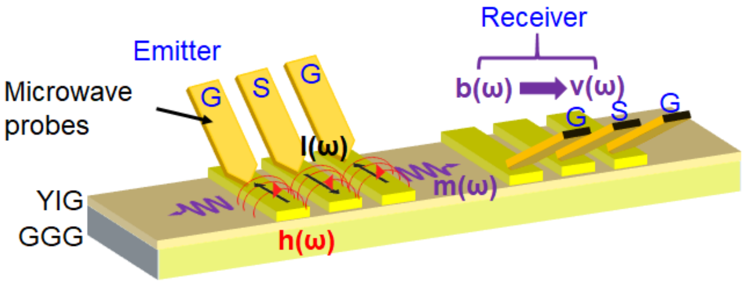

Figure 3.4: Two coplanar waveguides acting as microwave antennas are on top of a YIG thin film. $I(\omega)$ is the RF current that is injected in port 1 (Emitter). Microwave probes are used to drive the RF signal in the microwave antenna. This RF signal generates a microwave magnetic field $\vec{h}(\omega)$ which couples to the spins of the ferrimagnetic material under the transmission line. The magnetic interaction induces a dynamic magnetization component $\vec{m}(\omega)$. Spin precessional motion is created in the magnetically ordered material and this peturbation coherently propagates depending on the spin wave dispersion relation. The perturbation might reach the second integrated microwave antenna. Here due to $\vec{m}(t)$ a time-dependent magnetic field $\vec{b}(t)$ is active. Because of Faraday-Lenz law $\vec{b}(t)$ induces a voltage drop $v(t)$. The electrical signal is measured by means of microwave probes.

There is a wide range of literature explaining the physics of spin wave excitations by means of microwave antennas and their RF field. Here are cited references that have inspired the structuring and explanation of this section [Yu03], [Hub00], [Neu00], [Gie00], [Gur00], [Poz00].

The dynamics that is excited by the RF field is:

$$\vec{m}(\omega, t, \vec{r}, \vec{k}) = \vec{\chi}(\omega)\vec{h}(\omega, t, \vec{r}) \tag{3.3}$$

$\vec{\chi}(\omega)$ is the susceptibility tensor and it depends on the frequency ω. For a homogeneous magnetization RF field we discussed the relevant susceptibility tensor components in Eqs. 2.34 to 2.29 for a spherical sample. For simplicity of the following calculation we assume a homogeneous field. Because of precessing magnetization a variation in time of magnetic flux ϕ_{M} is sensed by the second antenna:

$$V_{\mathrm{ind}} = -\frac{d\phi_{\mathrm{M}}}{dt} \tag{3.4}$$

V_{ind} represents the electromotive force that is generated at port 2. Let us assume now that the RF field has only an in-plane component along y- axis $\xi(y)$ (simplified case). The integrated spatial distribution of the RF field is such that $\int \xi(y)dy = \Xi$. Introducing a constant C that depends upon CPW geometry and equilibrium magnetization direction with respect to x-axis the expression for magnetic flux can be elaborated from Eq.s 3.5 to 3.6:

$$\phi_{\mathrm{M}} = \mu_0 \int_{V_S} \vec{h} \cdot \vec{m} \frac{1}{I} dV. \tag{3.5}$$

$$\phi_{\mathrm{M}} = C \int \xi(y) m_y(y,t) dy. \tag{3.6}$$

In Eq. 3.5 V_S is the sample volume, I is the current flowing in the CPW at port 1.

Rearranging terms and using Eq. 3.3 the electromotive force (Eq. 3.4) in terms of the relevant parameters can be expressed as:

$$V_{\mathrm{ind}} \propto \int \xi(y) \chi_{yy} \frac{dh(y,t)}{dt} dy. \tag{3.7}$$

The Fourier transformed representation of Eq. 3.7 reads [Hub00]:

$$V_{\mathrm{ind}} \propto \int \rho(k) \chi_{yy}(k) h(k,\omega) dk. \tag{3.8}$$

$\rho(k)$ is the excitation spectrum of the microwave field, which is determined by microwave antenna's geometry as discussed in chapter 4.

The VNa detects V_{ind}. Coupling between microwave antenna and magnetic material is inductive, inductance matrix can be used to model system response [Vla00]. Following this formalism one can write for the reflected (a_{pp}) and transmitted (a_{pq} with $i \neq j$) signal:

$$a_{pp}(\omega) \sim \int \chi(\omega,k) \rho(k)^2 dk \tag{3.9}$$

$$a_{qp}(\omega) \sim \int \chi(\omega,k) \rho(k)^2 exp(-jkD) dk \tag{3.10}$$

The propagating signal accumulates phase over the travelled distance D according to Eq. 3.10.

3.1.6 Spin waves resonance and propagation

Spin waves are nonzero wave-vector excitations to the equilibrium magnetization. Propagating spin waves feature group velocity and attenuation length, which is linked to spin wave lifetime. The frequency linewidth of a spin wave resonance measured in an experiment as sketched in Fig. 3.4 reflects possible dissipation mechanisms of the system and the excitation spectrum of the coplanar waveguide.

Nonreciprocal propagation occurs for in-plane geometry excitation when $\vec{k}_{SW} \perp \vec{M}_{eq}$. It is determined by both the asymmetry that the dynamic dipolar field spatial profile features [Gla00] and the non-reciprocity of MSSW

We should now briefly examine all these physical quantities and Fig.s

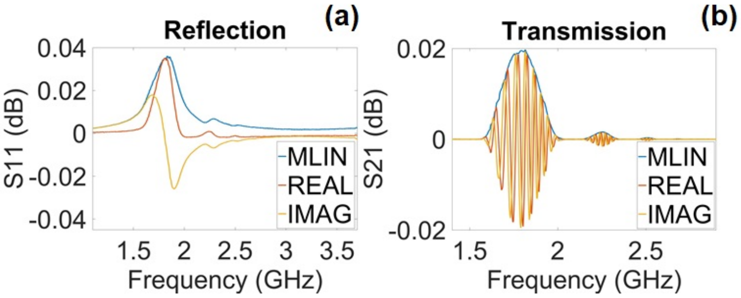

Figure 3.5: VNA spectra of magnetostatic surface spin waves in clean YIG. Applied static field $\mu_0 H_{\text{ext}} = 15$ mT is in-plane and perpendicular to SWs propagation. Power level of microwave signal $P_{RF} = -20$ dBm. . (a) Linear magnitude (MLIN), real part (REAL) and imaginary part (IMAG) of reflection parameter S_{11}. Each peak in MLIN corresponds to a resonance. (b) Linear magnitude (MLIN), real part (REAL) and imaginary part (IMAG) of transmission parameter S_{21}. Oscillating behavior of real and imaginary part is a signature of propagating spin wave.

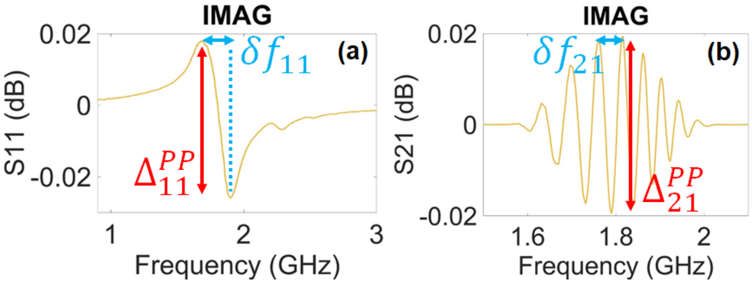

Figure 3.6: VNA spectra of magnetostatic surface spin waves in clean YIG. Applied static field $\mu_0 H_{\text{ext}} = 15$ mT is in-plane and perpendicular to SWs propagation. Power level of microwave signal $P_{RF} = -20$ dBm. frequency linewidth and peak-to-peak variation is illustrated for S_{11} and S_{21}. Peak-to-peak variation is calculated as difference in signal amplitude of maximum and minimum peaks. (a) Frequency linewidth is calculated as the frequency spacing between maximum and minimum of the signal. $\delta f_{11} = 0.204$ GHz, $\Delta_{11}^{PP} = 0.0441$ dB. (b) Oscillating signal is employed to evaluate group velocity for a selected resonant mode. Frequency spacing (δf) of two adjacent maxima is extracted. Same procedure can be applied for two adjacent minima. $\delta f_{11} = 0.055$ GHz, $\Delta_{11}^{PP} = 0.0389$ dB

We shortly discuss the relevant parameters and decribed them.

- *Group velocity.* It is the velocity with which a wave transfers energy. In a one-dimensional problem it is defined as:

$$v_g = \frac{d\omega}{dk} \tag{3.11}$$

  In 3D problems the equation is generalized replacing $\frac{d}{dk}$ with $\vec{\nabla}_{\vec{k}}$.

  In AESWS experiments the oscillatory part of real and imaginary voltage components at resonance can be used to estimate the group velocity. The frequency spacing (δf) between two adjacent maxima is related to a phase accumulation $\delta\Phi = 2\pi$ (refer to Fig. 3.7). This phase accumulation is observed at the receiver port and occurs over a distance equal to the separation (D) of the signal line of port 1 and signal line of port 2. We can therefore conclude [Yu01]:

$$v_g \approx \frac{2\pi(\delta f)}{2\pi/D} = (\delta f) \cdot D \tag{3.12}$$

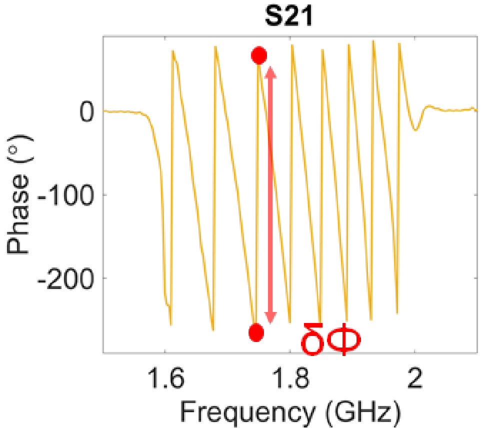

Figure 3.7: Phase measured for transmission parameter S_{21}. Static external field is $\mu_0 H_{\text{ext}} = 15$ mT. MSSW excitation, i.e. magnetization is in plane and perpendicular to SW propagation. Imaginary part of the same data set is shown in Fig. 3.6. Highlighted phase difference is $\delta\Phi = 342°$

- *Nonreciprocity factor* (β). Nonreciprocity depends on magnetic field ($\beta = \beta(\vec{H})$). Traveling signals can be related to transmission parameters through attenuation length (L_{SW}) and nonreciprocity factor [Yu01], [Neu00] [Schw00]. s is used to indicate the spatial coordinate along propagation axis. ΔS_{pq} with $p, q = 1, 2$ represents the experimentally extracted peak-to-peak variation of the imaginary part at resonance.

$$\begin{aligned} \frac{\Delta S_{21}}{\Delta S_{11}} &= \beta(\vec{H}) \cdot exp(-D/L_{SW}), \\ \frac{\Delta S_{12}}{\Delta S_{22}} &= (1 - \beta(\vec{H})) \cdot exp(-D/L_{SW}). \end{aligned} \tag{3.13}$$

  Solving the system of Eqs 3.13 for β one can finds:

$$\beta = \frac{\frac{\Delta S_{21}}{\Delta S_{11}}}{\frac{\Delta S_{21}}{\Delta S_{11}} + \frac{\Delta S_{12}}{\Delta S_{22}}} \tag{3.14}$$

- *Attenuation length, L_{SW}.* Following the discussion from the nonreciprocal factor extraction one can find L_{SW} solving the system of Eqs 3.13 for L_{SW}. Indeed once β is known it can be used to determine L_{SW}:

$$L_{SW} = -D \cdot \left[ln\left(\frac{\Delta S_{21}}{\Delta S_{11}} \cdot \beta \right) \right]^{-1} \tag{3.15}$$

- *Spin wave lifetime.* Knowing group velocity and L_{SW} for spin wave the characteristic relaxation time is estimated:

$$\tau_{SW} = L_{SW}/v_g \tag{3.16}$$

- *Frequency linewidth at resonance.* In [Vla00] a model for frequency linewidth is elaborated. Data analysis will be based on this model. Frequency broadening at resonance can be described as follows:

  $$(\delta f)_{tot} = 2\alpha f + \frac{1}{2\pi} v_g \delta k \tag{3.17}$$

  It consists in two terms: intrinsic damping ($2\alpha f$) and inhomogeneous broadening ($\frac{1}{2\pi} v_g \delta k$). The model can be generalized in:

  $$(\delta f)_{tot} = \delta f + \delta f_{ex} \tag{3.18}$$

  stating that there are both intrinsic (first term) and extrinsic (second term) contribution to resonant peak broadening.

  With regard to Eq. 3.17 intrinsic damping is described by Gilbert phenomenological theory of magnetic losses. It describes losses that depend linearly on the frequency f. The extrinsic contribution is due to a finite FWHM of the RF field distribution in $\vec{k}$-space. As it has been analyzed in chapter 4 $\vec{k}$ excitation spectrum of the microwave field that is generated by the coplanar waveguide features finite FWHM for each resonant mode.

  For an extensive analysis on magnetic damping the interested reader may refer to [Ari00], [Bab00].

3.1.7 Measurement methodology

The measured devices are presented in detail in chapter 4. In brief, two CPWs are fabricated on top of a ferrimagnetic 100 nm thick layer. The substrate is non magnetic and insulating.

VNA internal electronic circuit can be set to optimize signal detection at port 2 and signal generation at port 1 ("asymmetric jumper"), otherwise it can be configured to a symmetric electronic readout of signals ("symmetric jumper"). If not otherwise specified in the course of this thesis all VNA-AESWS data have been measured with asymmetric jumper.

The chip is muounted in the center of the sample stage. Microwave probes are borught into contact with the CPWs. The key parameter for VNA measurement is the RF power level. For the experiment the linear regime of magnetization oscillations needs to be ensured such that we used small power level.

For each scattering parameter, five quantities are measured: real part (REAL), imaginary part (IMAG), logarithmic magnitude, linear magnitude and phase.

The first step of every measurement is the acquisition of a reference spectrum at 90 mT in backward volume configuration or at 0 mT. For measurement settings (ii) and (iii) the reference signal is acquired at 0 mT. Subtracting a reference measurement increases signal-to-noise ratio. From reference subtraction a new linear magnitude ($MLIN$) for the generic S-parameter is calculated:

$$MLIN = \sqrt{(REAL_{meas} - REAL_{ref})^2 + (IMAG_{meas} - IMAG_{ref})^2} \tag{3.19}$$

Where $REAL_{meas}$ ($IMAG_{meas}$) indicates the real part (imaginary part) of the measured data set and $REAL_{ref}$ ($IMAG_{ref}$) is the real part (imaginary part) of the reference data set.

3.2 Brillouin Light Scattering

Brillouin light scattering spectroscopy is a method to optically detect spin waves (magnons) by analyzing the energy shift of inelastically scattered photons. It allows the study of both coherent and incoherent magnons, i.e. thermally excited magnons.

BLS allows for space and wave-vector-resolved mapping of spin waves. It enables real-time study of spin wave propagation with time-resolved measurement featuring ns resolution [Dem00].

In this section we introduce the underlying physics of BLS spectroscopy on magnons and the setup

3.2.1 Inelastic light scattering

In a quasi-classical picture Brillouin Light Scattering (BLS) can be interpreted as Doppler shift which occurs through a time- and space-dependent potential that is determined by variations of the dielectric tensor of the medium. These variations are caused by propagating spin waves via magneto-optic coupling. [Seb00].

In a quantum-mechanical picture BLS process involves scattering of photons with magnons as shown in Fig. 3.8. In this process energy and momentum are conserved [Seb00]. It is noted that BLS is a phase sensitive process.

Conservation laws are described as follows:

$$\begin{aligned} \hbar\omega_{out} &= \hbar\omega_{in} \pm \hbar\omega_{SW}, \\ \hbar\vec{k}_{out} &= \hbar\vec{k}_{in} \pm \hbar\vec{k}_{SW}. \end{aligned} \tag{3.20}$$

The '+' sign refers to magnon annihilation ("Anti-Stokes process"), whereas the '−' sign refers to magnon creation ("Stokes process").

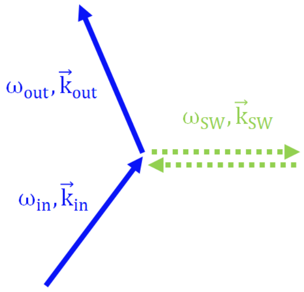

Figure 3.8: BLS scattering diagram. Incident photon (ω_{in}, $\vec{k}_{in}$) interacts with magnons exchanging momentum and energy. The scattered photon (ω_{out}, $\vec{k}_{out}$) yields energy and momentum that depend on scattering process according to Eq. 3.20. A magnon (ω_{SW}, $\vec{k}_{SW}$) can be created or annihilated upon scattering.

Exploiting the characteristics of BLS process information on frequency (energy) wave vector distribution and phase of magnons can be obtained.

During the course of this the spatially resolved BLS measurements were mainly conducted as discussed in the following sections.

Interested readers may find further details in [She00], [Wet00], [Coc00].

3.2.2 Experimental setup of microfocused BLS

Two components are essential for BLS spectroscopy: (i) a monochromatic light source and (ii) high contrast interferometer [Seb00].

We use a laser at $\lambda = 473$ nm with a narrow spectral linewidth ($\lesssim 10$ MHz) is used. Laser power is adjusted to minimize optically induced heating using an attenuator. Typical laser power is $\lesssim 1$ mW.

Tandem Fabry-Perot Interferometer (TFPI) is the experimental tool for high contrast frequency analysis. It consists of a set of two Fabry-Perot Interferometers (FPI). An FPI is an interferometer with two highly semitransparent mirrors that are mounted accurately parallel to each other. Constructive interference occurs for a mirror distance which is a multiple of half of the wavelength. Therefore transmission is periodic in the spacing between the two mirrors.

During measurements, the wavelength/frequency of scattered light is analyzed by sweeping the mirror distance. Frequency analysis to determine spin wave frequency is performed by comparison of the mirror spacing referring to scattered light to mirror spacing for transmission of a reference light beam that enters TFPI without any interaction with the sample.

The entire optical setup is hosted on an optical table for vibration damping. An objective lens focuses the incoming laser light on the sample. Laser spot diameter is ~ 350 nm. Sample mounting is done with accuracy to ensure mechanical stability.

Given the setup geometry, maximum magnetic field for Damon-Eshbach excitation geometry is 100 mT and for Backward-Volume excitation geometry is 200 mT. Fig. 3.9 illustrates the BLS setup at LMGN.

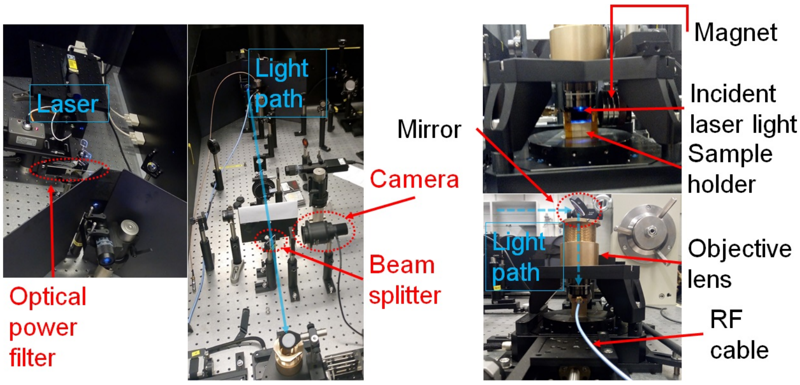

Figure 3.9: Pictures of BLS setup LMGN at EPFL. The entire experimental setup rests on an optical table for vibration damping. A continuously variable reflective neutral density filter from Thorlabs is used to adjust laser power. Light is directed towards the sample with a system of mirrors. Last optical for focusing is the objective lens. Chip is mounted on a brass block. The chip support is integrated with a RF connector so that a microwave cable can drive a RF signal in the device. A movable magnet provides the chosen field within speficied limits. Light path from the laser to the sample is indicated with a light blue arrow. Light wavelength is $\lambda = 473$ nm with laser spot size at the sample position of ~ 350 nm. Investigated sample and laserspot can be observed with a camera.

3.2.3 Measurement methodology

Goal of the analysis is to explore the impact of nanoparticles on SW propagation properties of YIG. Thermally- and microwave-excited magnons are measured.

- *Thermally excited magnons in YIG.* For YIG a large number of magnons is excited at room temperature (300 K). Thermal energy for excitation can be estimated to be $\sim \kappa_B T \approx 4 \times 10^{-21}$ J and magnon energy can be estimated to be $\sim \hbar\gamma\mu_0 M_\mathrm{S} \approx 1 \times 10^{-34}$ J [Wet00]. As thermal energy is orders of magnitude greater than typical magnon energy in YIG a large number of incoherent magnons is excited

- *Microwave excited magnons in YIG.* To excite magnons via RF signal the chip is glued with silver paste on a coplanar waveguide (Fig. 3.10). Transmission lines are electrically connected to device ground and signal lines with wire bonding. Bonded wires are made of aluminum with 33 μm diamater. From a LabView program the microwave excitation signalis configured setting power level and frequency. When analyzing data the BLS signal is integrated and then it is studied as function of the injected microwave signal frequency. The frequency interval for which BLS counts are acquired by the system at each excitation frequency can be tuned. For every excitation frequency the sum of all counts within the chosen frequency interval is computed and the outcome is the integrated BLS signal.

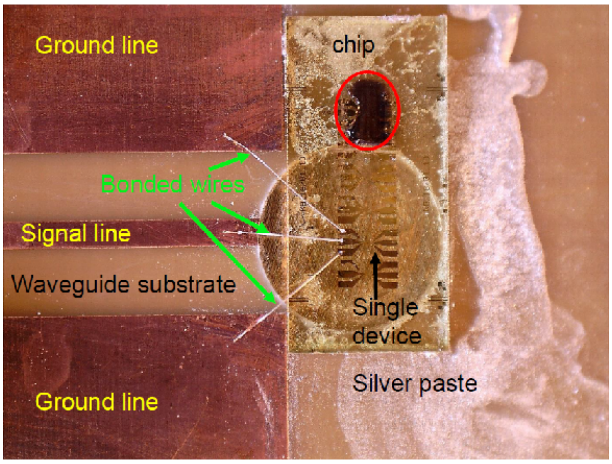

Figure 3.10: Photograph of glued and wire-bonded chip. Chip is glued with silver paste to waveguide substrate. Aluminum wires are used to bond ground and signal lines to corresponding lines of a CPW on a substrate. The substrate features a hole that matches the area of the bonded device. It allows to shine laser light from the backside to access SWs underneath the integrated CPW. enhance backreflection thus signal-to-noise ration during measurement. The red circle highlights the dried droplet of nanoparticles solution.

4. Sample description

4.1 Coplanar waveguide structure

A coplanar waveguide can be divided up in three regions: (i) *contact region*, where microwave tips are landed on contact pads to establish electrical contact at high frequency, (ii) *taper region* to transfer signal from contact region to (iii) *transmission region* which is where microwave signal excites spin-precessional motion within functional medium [Hub00].

Devices that are discussed in this thesis feature the following design:

- signal and ground lines width $W_S = W_{GR} = 2.9\,\mu m$
- gap width between strips $W_g = 0.7\,\mu m$
- thickness $t = 0.1\,\mu m$

Parameters' naming is taken after Fig. 3.3. The coplanar waveguide is fabricated from gold on 100 nm thick yttrium iron garnet ($Y_3Fe_5O_{12}$, YIG) film. The YIG was grown by liquid phase epitaxy (LPE) on a gadolinium gallium garnet ($Gd_3Ga_5O_{12}$, GGG) substrate (500 μm thick). YIG is then patterned to form mesas with slanted edges to minimize spin wave reflection.

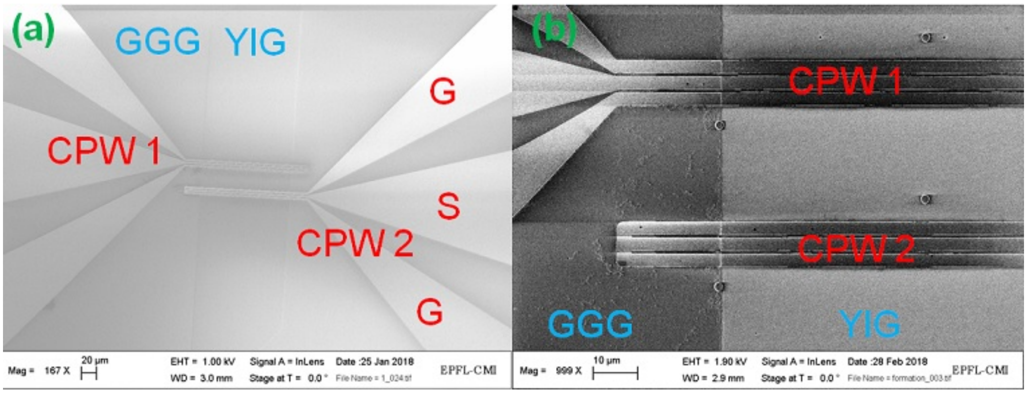

Figure 4.1: SEM images of a device. On top of YIG gold coplanar waveguides are fabricated. (a) Taper region and (b) central region showing two ground lines and signal lines.

4.2 RF field distribution

COMSOL Multiphysics software simulation is employed to extract the spatial profile of the microwave field that is generated by the coplanar waveguide. The simulated system (Fig. 4.2) is a simplified model of the actual device. A cross section of the transmission line is built on top of a substrate that has the dielectric constant of GGG. An air environment is simulated around the CPW. The extracted microwave field spatial profile is illustrated in Fig. 4.3.

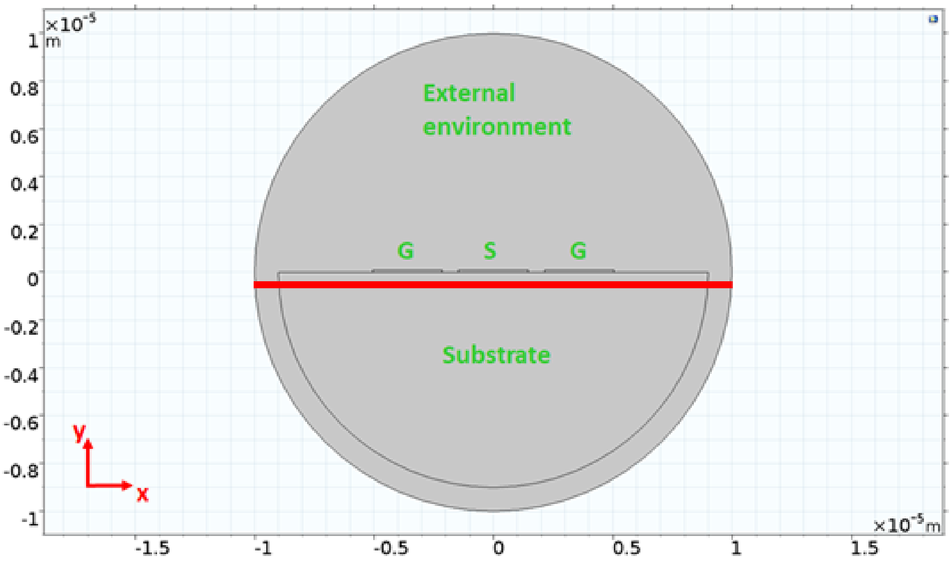

Figure 4.2: Model for COMSOL simulation, cartesian axes are shown at the left bottom part of the picture. Signal line width is 2.92 μm and ground line width is 2.90 μm. Conductive lines thickness is 100 nm. Gap width between edges of adjacent conductive strip is 0.7 μm. The substrate has dielectric constant ϵ_r of GGG which is $\epsilon_r = 12$. External environment is modeled as air. CPW is indicated by three labels: 'G' for ground lines and 'S' for signal line. Microwave field is generated for 5 GHz signal. Skin effect is not important in this regime. Skin depth is given by this formula $\delta(f) = \sqrt{\rho/(\pi f \mu)}$; with ρ being the resistivity and μ the magnetic permeability. For gold skin depth at 5 GHz is $\delta \approx 1$ μm, i.e. one order of magnitude larger than waveguide's thickness. The solid red line is used to extract the profile of the microwave field (see Fig. 4.3)

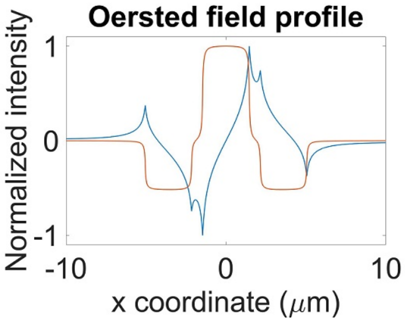

Figure 4.3: Spatial profile of microwave field that is generated by coplanar waveguide. Spatial profile is taken 1 nm below interface CPW/substrate (see red solid line in Fig. 4.2). Microwave signal frequency is oscillating at 5 GHz. In-plane (red solid line) and out-of-plane (blue solid line) components of the CPW generated microwave field are plotted.

Fig. 4.4 displays the Fourier analysis of the in-plane component of Fig. 4.3 (black curve). FFT algorithm is applied to obtain $\vec{k}$ distribution of microwave field. Each peak represents a wave-vector that can be excited by the microwave field.

The main peak is centered at $|\vec{k}'_{1,fit}| = (0.7937 \pm 0.0005)$ rad/μm and has a FWHM $\Delta k'_{FWHM} = (0.8518 \pm 0.0034)$ rad/μm. The excitation of this geometry is adequate to perform VNA-AESWS. The microwave antenna excites non-zero wavevectors with a finite FWHM. This allows to probe the magnetization dynamics of the sample by propagating spin waves. The broadening of the peaks in the $\vec{k}$ distribution of the excitation spectrum will cause a broadening of the resonance peak in the frequency domain as discussed in Sect. 3.1.6 (Eq. 3.17).

The spatial profile of the microwave field for $20\,\mu$m is shown for comparison (red line in Fig. 4.4). Executing gaussian fit of the most prominent peak one obtains $|\vec{k}_{1,fit}| = (0.101 \pm 0.002)\,$rad/$\mu$m and an estimated FWHM $\Delta k_{FWHM} = 0.097\,$rad/$\mu$m. Here $\vec{k}_1$ is close to zero wave-vector i.e close to the condition of FMR

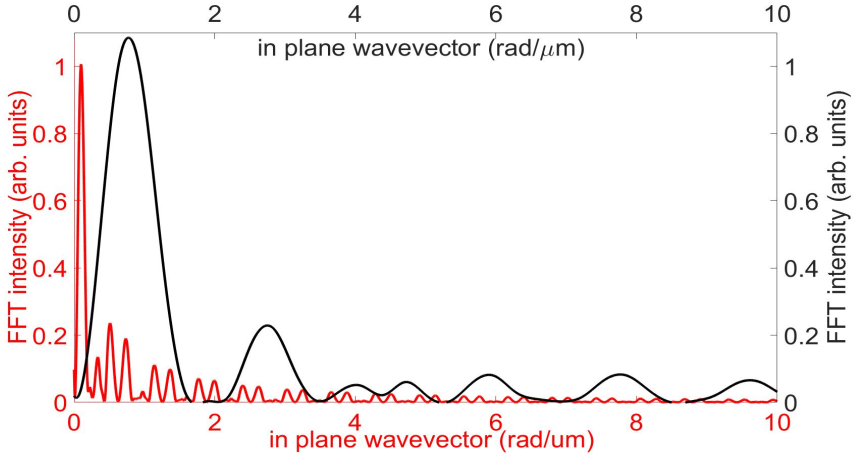

Figure 4.4: Coplanar waveguide intensity distribution. Spatial profile of Oersted field $\xi(x, y)$ from microwave antenna is extracted from COMSOL simulation. In-plane wavevector distribution is presented for $W_S = 20\,\mu$m (red solid curve) and $W_S = 2\,\mu$m (black solid curve). Each peak represents wave vectors that can be excited by the microwave field. For case (ii) lowest mode is non zero and each peak has finite non-zero full width at half maximum (FWHM).

5. Magnetic Nanomaterials

This chapter provides an overview on the magnetic nanoparticles (NPs) that are used to investigate NP induced scattering of SWs in YIG.

5.1 Nanoparticles

Iron oxide nanoparticles featuring different average sizes allow us to investigate the impact of NPs on YIG magnetization dynamics for different magnetic regime, i.e. superparamagnetic and ferrimagnetic [Kef00].

Barium and strontium ferrite belong to the category of *hexaferrite* compounds [Pul00]. They exhibit large (> 1 T) magnetocrystalline anisotropy field. This leads to high frequency ($\gtrsim$ 50 GHz) ferromagnetic resonance at zero applied magnetic field.

We are interested in (i) exploring the coupling of these nanoparticles with magnons in YIG and in (ii) studying methods to excite resonant modes of hexaferrite nanoparticles to extend the grating coupler effect to high frequency. Due to time restrictions the thesis work mainly focused on (i); comments on (ii) will be made in 7.2.

5.1.1 γ-Fe$_2$O$_3$ nanoparticles

The study of γ-Fe$_2$O$_3$ (maghemite) nanoparticles has been enabled by a collaboration with Prof. H. Hofmann and the Laboratory for Powder Technology (*LTP*). We received suspensions of maghemite. Their NPs preparation and properties are discussed in [Bon00].

NPs were created with both cubic (average size $\sim$ 20 nm) and spherical shape (average size $\sim$ 10 nm). To reduce nanoparticles' aggregation two suspensions were made with coated nanoparticles. The outer shell of NPs was formed by caffeic acid coating.

Given the average size of these nanoparticles they feature a blocking temperature $T_B = 250 \div 300$ K. Saturation magnetization amounts to $M_\mathrm{S} = 72$ A·kg^{-1}·m^2 (per density unit) [Bon00].

We imaged with a Transmission Electron Microscope (TEM) (Fig. 5.1).

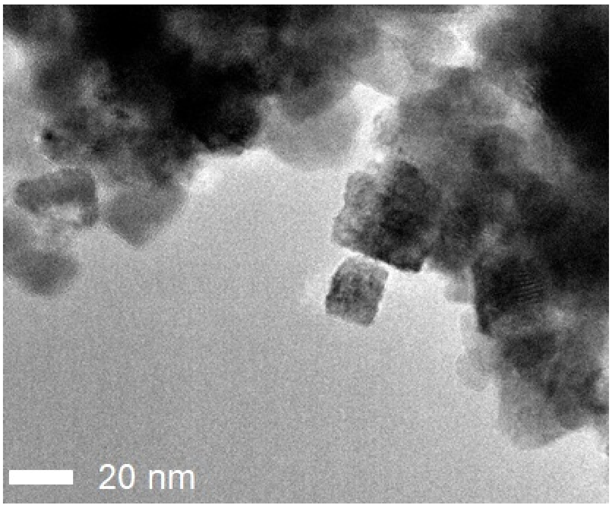

Figure 5.1: Maghemite nanoparticle on a standard TEM grid. Scale bar (white stripe at center bottom position) is 20 nm. Nanoparticles are organized in clusters. Cubic shape is clearly observed in nanoparticles at the edge of the agglomerate. Typical size of nanoparticles according to TEM inspection is approximately $20nm$.

5.1.2 Hexaferrite materials

Barium ferrite ($BaFe_{12}O_{19}$) and Strontium ferrite ($SrFe_{12}O_{19}$) have M-type crystal structure [Pul00], [Cao00].

We used barium and strontium ferrite nanopowder to prepare suspensions. Hexaferrite suspensions were prepared in the laboratory LTP following the safety regulations of EPFL. We then characterized them with a TEM (Fig.s 5.2, 5.3)

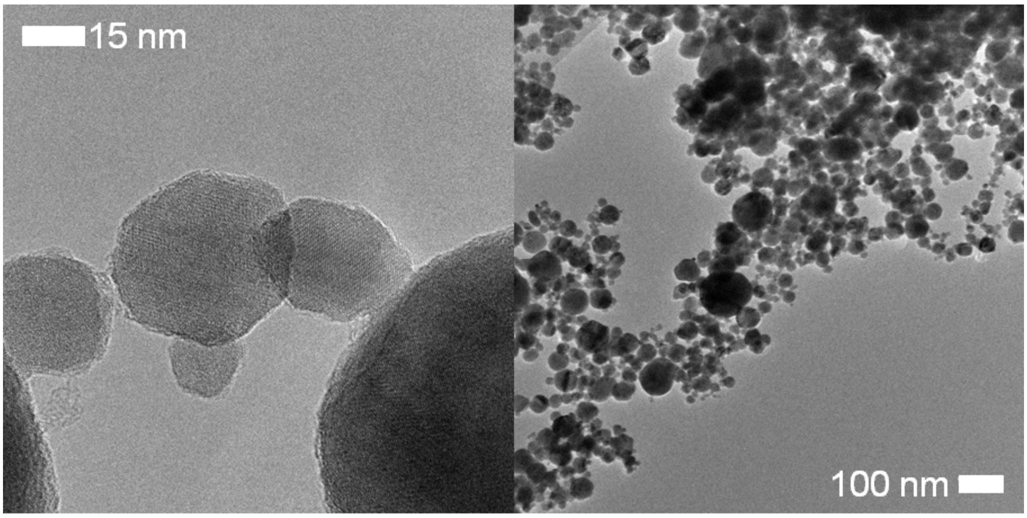

Figure 5.2: **Barium ferrite** suspension deposited on a TEM grid. Barium ferrite TEM investigation was performed thanks to a collaboration with C. Schillai, PhD student at LND lab of EPFL. Particles' diameter amount to 15 ÷ 20 nm, clusters are formed with a typical size of hundreds of nm.

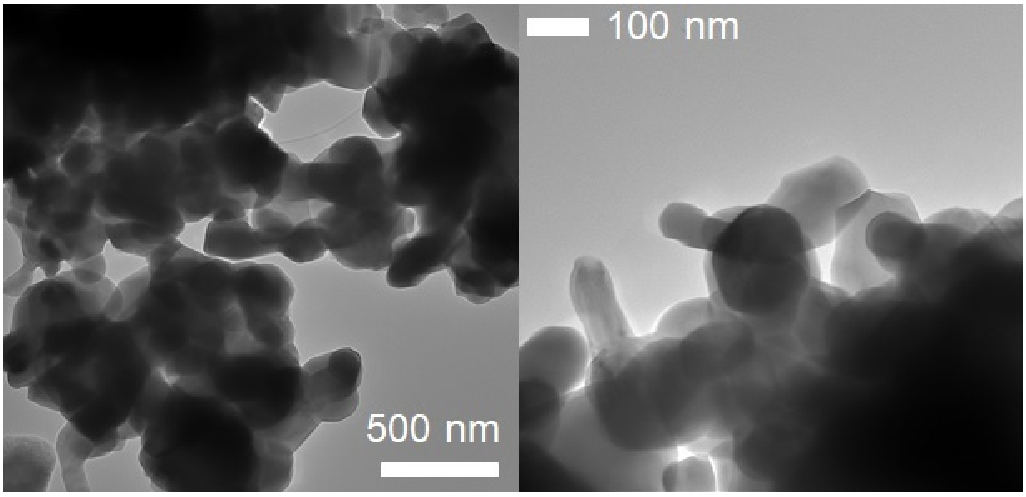

Figure 5.3: **Strontium ferrite** suspension deposited on a TEM grid. Clusters are formed in with characteristic size of $\gtrsim 1\,\mu$m.

5.2 Suspensions

Different solvents and concentrations have been tested in the course of this thesis; we focus on the suspensions that were then studied in experiments.

5.2.1 Colloidal suspensions: preparation methodology

- Iron oxide based NPs. The suspension with Fe_2O_3 NPs is treated in an ultrasonic bath. This step helps increase the homogeneity of the dispersion. With a pipette a droplet is extracted from the suspension and added to another container that has been previously filled with the selected solvent with desired quantity. Solvent quantity is measured with a scale (uncertainty ±0.05 mg). Ultrasonic excitation is used to mix the NPs in the solvent.

- Hexaferrite nanopowders. The scale is used to measure the required quantity of nanopowder (10 mg). Deionized water is poured in the same container with a pipette. The dilution factor of hexaferrite suspensions is 1000, i.e. approximately 10 mg of nanomaterial is dispersed in 10 g of solvent. The suspensions were prepared in the laboratory of LTP following the safety regulations of EPFL.

5.2.2 Deposition methods

This section describes methods that are used to deposit nanoparticles on YIG. Two deposition techniques have been adopted:

A. *Strontium ferrite (SrM) nanoparticles.* Approximately 10 μL of nanopowder suspension is deposited on chip fully covering its surface. Drying process occurs at room temperature.

   The clean device that is measured before NPs deposition is referred to as **YIG1**. The same device that is measured after deposition of SrM NPs is named **YIG1-SrM**.

B. *Maghemite nanoparticles.* Maghemite with caffeic acid coating has been investigated. To deposit NPs the entire chip is immersed in a bath containing nanoparticle suspension ($\sim$ 3 mL). Volume dilution factor is $1 : 10^9$ and deionized water is used as solvent. Chip is let in the suspension bath for 40 min. During this time a DC current $I_{DC} = 10$ mA is applied to one CPW. The intent was to explore the influence of static magnetic field on the nanoparticles deposition. After 40 minutes the suspension is removed from the container and chip dries at room temperature.

   The clean device that is measured before NPs deposition is referred to as **YIG2**. The same device that is measured after deposition of maghemite NPs is named **YIG2-γFe$_2$O$_3$**.

Strontium ferrite distribution on YIG has been investigated by SEM technique and few images are reported in chapter 6 to clearly discuss BLS data.

A more detailed characterization was needed to understand the outcome from (B) maghemite deposition. We report here images of the SEM and AFM characterization.

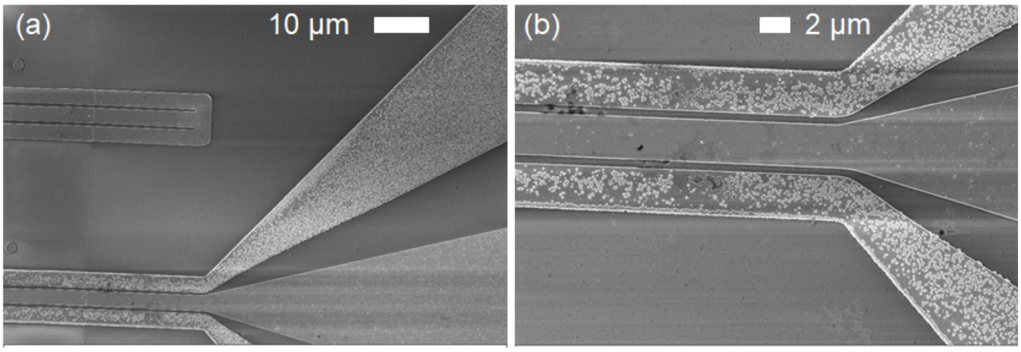

Figure 5.4: SEM images of CPWs after nanoparticle deposition. Distribution of CPW coverage is dense in the contact pads area. Ground pads are highly covered. On the contrary signal line has very low coverage. This distribution is attributed to the application of the DC current. The caffeic acid coating has hydroxilic groups at the end of the carbon chain. Therefore the electrostatic interaction with hydroxilic groups may have caused this distribution pattern. (a) CPW pad. (b) Ground and signal lines near the YIG mesas edge; concentration of coverage is gradually reduced as one moves along the signal line.

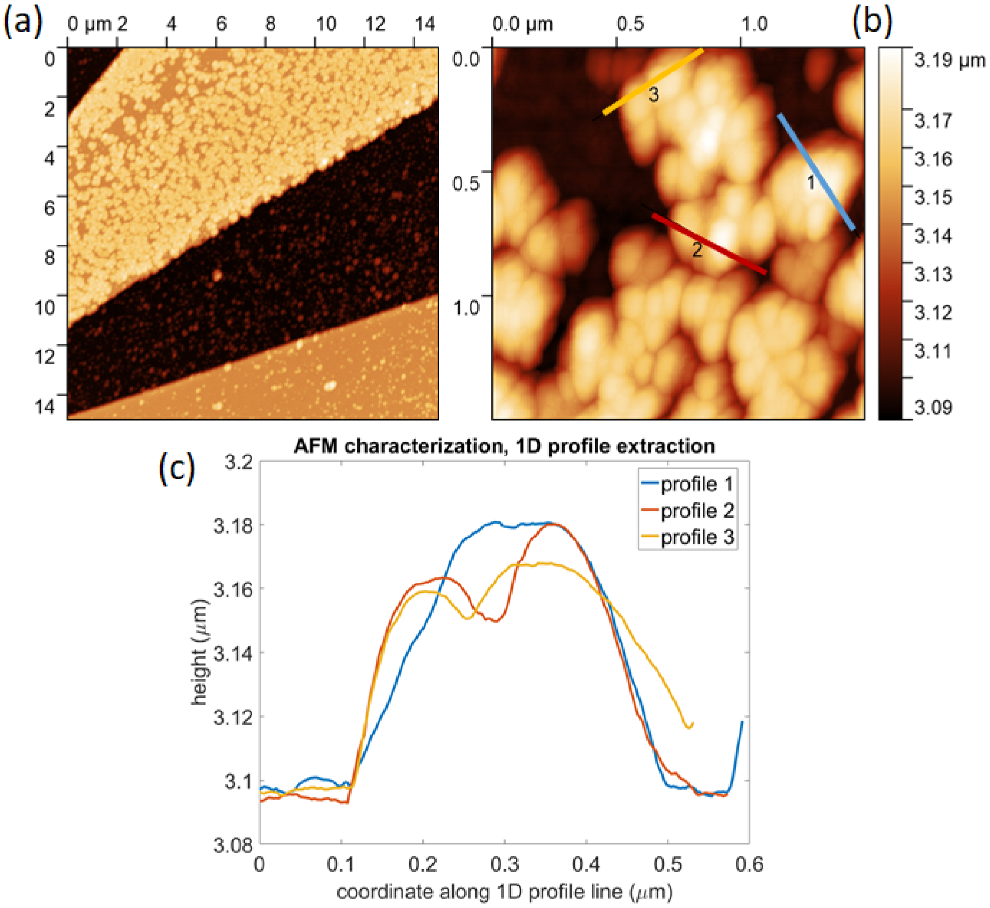

Figure 5.5: AFM images of CPW that is shown in Fig.5.4. AFM tip has radius $R < 5$ nm. (A) Area between ground pad and signal pad is imaged, decoration is higher on the pads. (B) Detailed imaged of area between ground and signal pad. Coverage is maximum pads. (C) Profile extraction for height measurement. Nanoparticles average size is 20nm [Bon00] this is in good agreement with measured height from extracted profile.

From AFM characterization we have found a typical height of the nanostructures decorating the CPW that matches the dimensions that are observed with TEM ($\sim 20nm$) (see Fig. 5.1).

6. Experiments

The scattering of SWs in YIG from NPs has been explored by means of broadband spin wave spectroscopy and Brillouin light scattering. Changes in spin wave propagation properties are the main interest in our study.

6.0.1 General comments on VNA measurements

- VNA spectra were acquired in Damon-Eshbach (DE) configuration (see section 2.4.2). This magnetostatic mode is surface-localized hence it is expected to be the most sensitive to the presence of nanoparticles deposited on YIG thin film.
- VNA internal electronic configuration is set for optimized signal emission from port 1 and optimized signal detection from port 2 ('asymmetric jumper' see section 3.1.7). Therefore S_{11} and S_{21} are analyzed.
- To enhance the signal-to-noise ratio the reference is chosen to be acquired at 90 mT on backward volume configuration. In MBVSW mode the torque that is exerted by microwave field of the CPW on the spins of the ferrimagnetic layer is minimum. In this manner the impact of unwanted torque and signal distortion on the measurement.
- To increase signal contrast data taken for successive field values during sweep are subtracted to each other. For two swept field values H_i and H_{i+1} one computes $\delta S_{pq} = S_{pq}(H_i) - S_{pq}(H_{i+1})$, with $p, q = 1, 2$. This procedure is referred to as *neighboring subtraction*.
- The data analysis focuses mainly on changes in the linewidth of the resonance peak. This can relate to surface scattering that is enhanced at sites where NPs are deposited.

6.1 Samples YIG1 & YIG1-SrM

Strontium ferrite suspension based on deionized water has been deposited via drop-casting on the chip. The droplet dried at room temperature. TEM characterization has shown that strontium ferrite form clusters with micrometer sizes.

6.1.1 VNA measurements - YIG1 & YIG1-SrM

Measurements are conducted using signal microwave power $P_{RF} = -20$ dBm. This guarantees linear regime for SWs excitation.

Magnetostatic surface wave mode excitation

Fig. 6.1 illustrates scattering parameters δS_{pq} in reflection and transmission configuration on clean YIG (sample YIG1) and after deposition of SrM nanoparticles (sample YIG1-SrM).

Spectra δS_{21} show different behavior for negative and positive fields H. This is due to nonreciprocity of spin wave propagation for this type of excitation geometry. The finite resonance at $H = 0$ of 0.57 GHz indicates that the YIG exhibits a magnetic ansisotropy that does not originate from shape anisotropy alone and enter the effective field Eq. 2.16

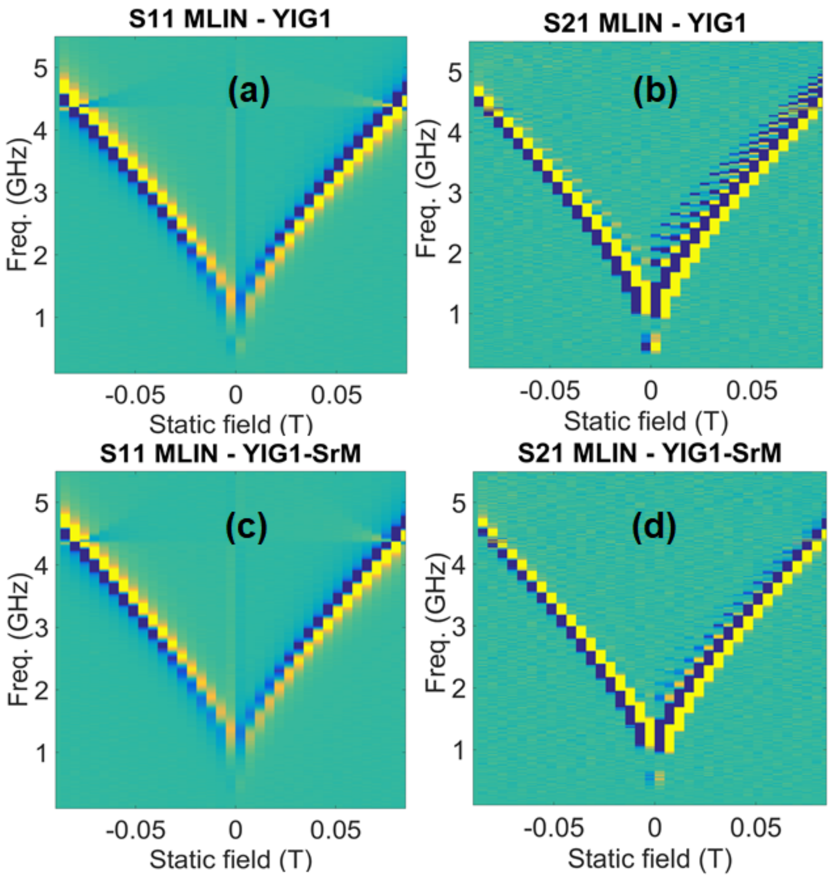

Figure 6.1: Color coded graphs showing (a) δS_{11} and (b) δS_{21} obtained on bare YIG: sample YIG1; (c) δS_{11} and (d) δS_{21} obtained on YIG decorated with SrM NPs: sample YIG1-SrM. Signals. In (b) we observe non-reciprocity i.e. for $H > 0$ more resonant mode, propagating between the CPWs, are found compared to $H < 0$. Comparing (b) and (d) the signal of higher frequency modes is reduced for $H > 0$ in case of YIG containing NPs.

The data S_{11} for the clean device (YIG1) and device after deposition (YIG1-SrM) are used to extract gyromagnetic ratio ($\frac{\gamma}{2\pi}$) and effective magnetization (M_{eff}). Using Eq. 2.49 we analyze the relation $f_{res}^2 - H_{\text{ext}}$. Assuming a fixed wave vector, we are interested in the first resonant mode, we evaluate the dependence of the resonant frequency as the field is swept. If one squares Eq. 2.49 and expresses ω_{H} and ω_{eff} in terms of H and M_{eff} finds a relation of this type $f_{res}^2(H) = a_2H^2 + a_1H + a_0$, with $f_{res} = \frac{\omega_{res}}{2\pi}$ (see Fig. 6.2). Results are in Tab. 6.1.

Parameter	sample YIG1	sample YIG1-SrM
$\frac{\gamma}{2\pi}$ (GHz/T)	29.5 ± 0.7	29.7 ± 1.0
M_{eff} (mT)	173.6 ± 6.3	171.9 ± 8.7

Table 6.1: Extracted parameters $\frac{\gamma}{2\pi}$ and M_S from S_{11} spectra.

.

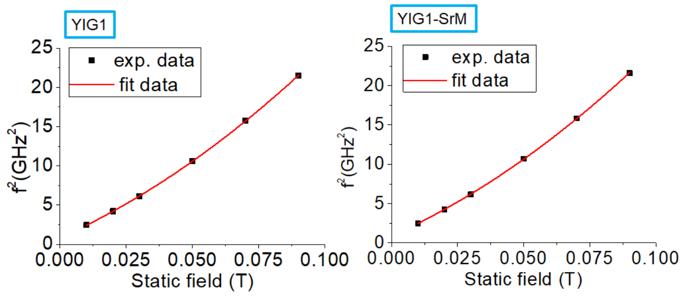

Figure 6.2: Experimental data from S_{11} linear magnitude in magnetostatic backward volume mode configuration. Fit function is taken after Eq. 2.49

The fitted values for the gyromagnetic ratio are higher than the value 28.3 GHz/T reported for YIG in Ref. [Mae00]. The analysis of data taken in MSBVW (refer to Fig. 6.3) configuration yields $\frac{\gamma}{2\pi} = 28.4$ GHz/T (Tab. 6.2).

Parameter	sample YIG1	sample YIG1-SrM
$\frac{\gamma}{2\pi}$ (GHz/T)	28.4 ± 1.1	28.4 ± 1.3
M_{eff} (mT)	173.2 ± 10.5	171.9 ± 12.4

Table 6.2: Parameters extracted from linear magnitude of S_{11} in magnetostatic backward volume mode configuration.

.

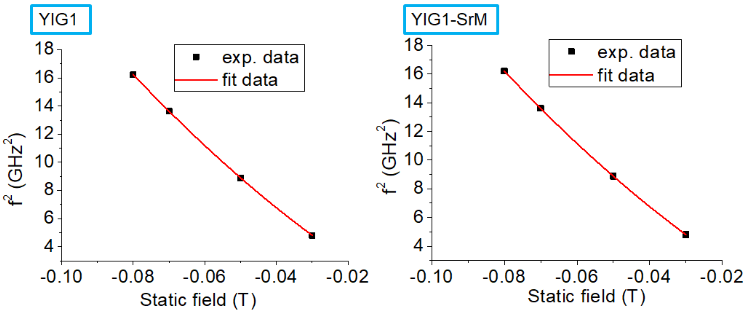

Figure 6.3: Experimental data from S_{11} linear magnitude in magnetostatic backward volume mode configuration. Fit function is taken after Eq. 2.51.

For both fitting analysis after NP deposition a slight increase of the relative error for the estimation of the parameters is observed. In general data taken in MSBVW configuration feature larger relative error than data acquired in MSSW.

Data in Tab. 6.2 are in better agreement with literature values. Moreover combining a comparison of resonant frequencies at 90 mT and at 100 mT with Kalinikos Slavin model and resonances that are observe with BLS measurements (see sub section 6.1.2) data in Tab. 6.2 provides a better description of our observations. The VNA measurement could suffer of deviation of the actual field from the nominally applied one. This is mainly due to chip positioning in the sample housing. If the chip position can not exactly reproduce the position that the Hall Sensor had while doing field calibration this will create a field variation.

This does not influence linewidth analysis. We study the linewidth dependence on resonance frequency. Focusing on resonance frequency takes already into account the static applied field mismatch.

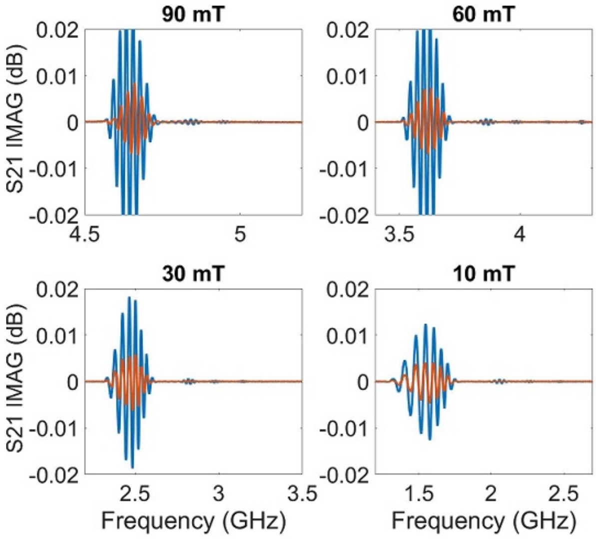

Figure 6.4: Imaginary part of transmission scattering parameter S_{21} displayed for selected fields. Blue curves represent sample YIG1 whereas red curves refer to sample YIG1-SrM. Oscillating behavior of imaginary part is signature of a spin wave resonance (SWR). The value of static field is indicated on top of each plot.

For sample YIG1-SrM the oscillation amplitude is reduced. We could argue that the presence of SrM cluster, because of its stray field and the randomly distributed anisotorpy axis, modifies the external field parameter that enters Eq. 2.50.

The imaginary part of reflection parameter is displayed in Fig. 6.5

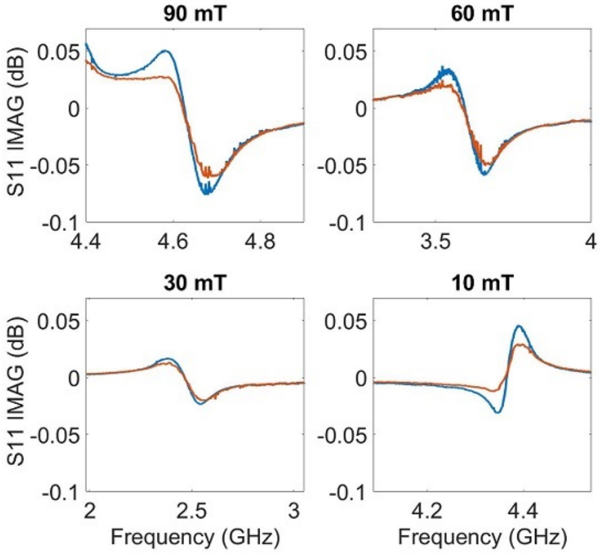

Figure 6.5: Imaginary part of transmission scattering parameter S_{11} displayed for selected fields. Blue curves represent sample YIG1 whereas red curves refer to sample YIG1-SrM. Oscillating behavior of imaginary part is signature of a spin wave resonance (SWR). The value of static field is indicated on top of each plot.

Signal attenuation is observed in spectra of Fig. 6.5. We interpret this effect as consequence of the stry field of SrM cluster.

The first resonant mode in magnetostatic surface mode excitation for S_{11} and S_{21} is studied to extract the linewidth.

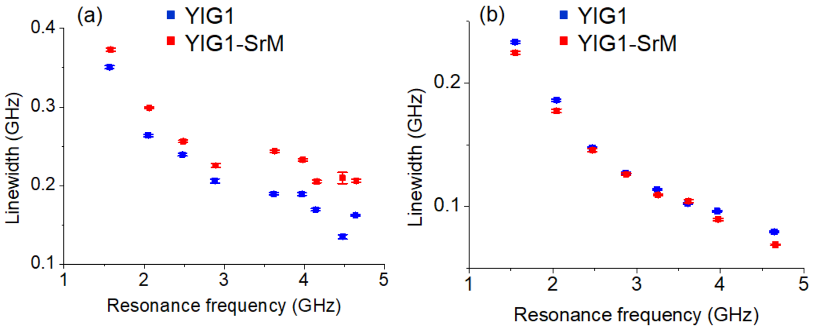

Figure 6.6: Frequency linewidth as function of resonant frequency.(a) Reflection parameter S_{11}; (b) transmission parameter S_{21}. This process is repeated at different static field. This analysis applies for clean device and after deposition device.

For reflection measurement the linewidth is broader after depositing nanoparticles on the device. Linewidth broadening in case of conserved length of magnetization vector leads to a reduction in signal strength. Following the discussion on susceptibility tensor in chapter 2 one can prove that $\Delta f \cdot \chi'_{res} \sim |\vec{M}|$, with Δf being the linewidth at resonance and χ'_{res} the real part of susceptibility at resonance.

For the peak width analysis (envelope function) of S_{21} we do not find a significant change in width Fig. 6.6.

In Fig.s6.6(a),(b) the evaluated linewidths decrease with increasing frequency. This indicates that the intrinsic Gilbert damping term is not relevant (refer to Eq. 3.17). Instead the extrinsic term with v_g is considered to be dominant. Derivating Eq. 2.49 it is shown that in the dipolar regime $v_g = \frac{d\omega_{\text{eff}}^2}{4\omega} e^{-2k_{\text{inp}} d} \propto \omega^{-1}$ motivating the observed behavior.

6.1.2 BLS measurements - YIG1-SrM

With BLS we have performed measurements using illumination (i) from the top side and (ii) from the back side of YIG. Laser wavelength is $\lambda_L = 473$ nm.

Top side illumination

In this geometry laser light is shone on YIG. Incoming photons can directly interact with YIG layer and/or strontium ferrite nanoparticles.

Laser power is set to ≈ 0.5 mW.

BLS on thermally excited magnetization dynamics

Spectra on thermally excited magnetization dynamics are shown in Fig. 6.7. The spectra are acquired at 100 mT and at 10 mT. Fig. 6.7 shows spectra for the Stokes signal.

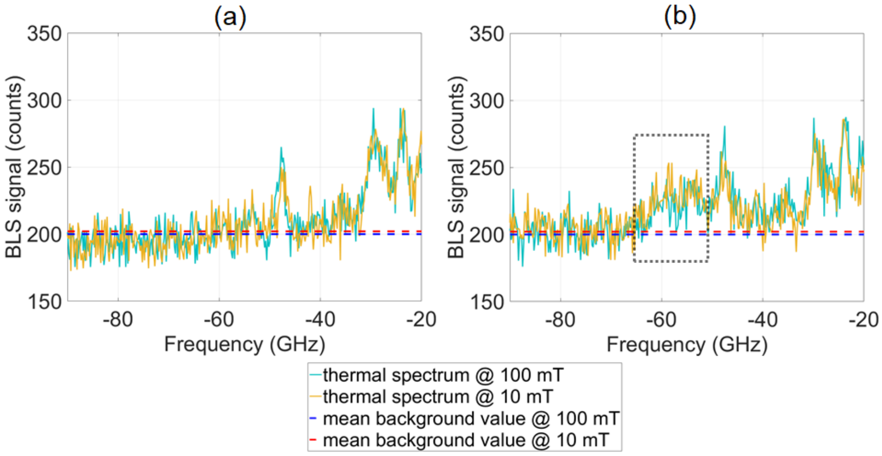

Figure 6.7: (a) Thermal spectra (Stokes signal) when laser was on bare YIG for 100 mT and 10 mT. (b) Thermal spectra (Stokes signal) when laser was on SrM cluster on YIG for 100 mT and 10 mT. Horizontal lines represents mean background value of signal at the fields. The interesting region of the spectrum is highlighted by the dotted box. (a),(b) Peaks outside the box are due to a laser mode and thermally excited magnons in YIG.

Peaks that are seen at frequencies below $\lesssim 48$ GHz are due to laser side bands. The interesting part of these spectra is the broad peak approximately centered at 60 GHz. Assuming an anisotropy field of 2 T ([Pul00]), neglecting the contribution of both the applied field and saturation magnetizations from Eq. 2.40 resonant frequency is roughly $f \approx \frac{\gamma}{2\pi}\mu_0 H_{ani} \simeq 57$ GHz.

Thermal spectra are fitted assuming the presence of two peaks (Fig. 6.8). Table 6.3 summarizes fit results

Static field (mT)	$\lvert f_1 \rvert$ (GHz)	σ_{f_1} (GHz)	Δf_1 (GHz)	$\sigma_{\Delta f_1}$ (GHz)	$\lvert f_2 \rvert$ (GHz)	σ_{f_2} (GHz)	Δf_2 (GHz)	$\sigma_{\Delta f_1}$ (GHz)
10	58.8	5.5	6.5	1.6	53.2	3.0	3.5	1.0
100	59.6	3.0	3.5	1.0	54.0	2.7	3.1	0.6

Table 6.3: Central frequency and Full Width at Half Maximum (FWHM) extracted for the two assumed peaks from the fitting. Δf_1 and Δf_2 are respectively FWHMs of resonance frequencies f_1 and f_2. Statistic error from fit is reported as σ_f for peak frequency and as $\sigma_{\Delta f}$ for FWHM.

.

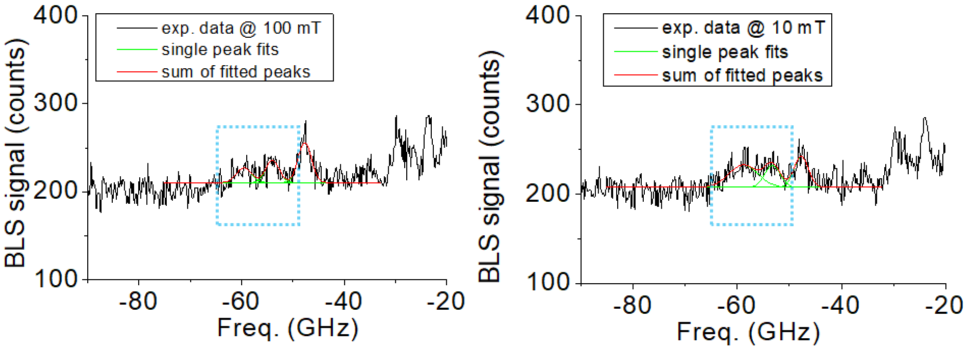

Figure 6.8: BLS signals from thermally induced magnetization dynamics in SrM clusters at 100 mT and at 10 mT. Raw BLS signals are fitted to extract peak frequency and FWHM (Tab. 6.3). Peak outside dotted box is due to laser mode.

From table 6.3 it can be noticed a shift to larger frequency values for a large field. The field variation that we applied induces a small effect compared to the typical linewidth that strontium ferrite could have according to section 2.3.2 (Eq.2.42). Strontium ferrite feature magnetocrystalline anisotropy field $\sim$ 2 T [Pul00]. Linewidth for a single crystal hexaferrite have been reported. For the case of barium ferrite ($BaFe_{12}O_{19}$) a linewidth of $\approx$ 25 Oe at 60 GHz was found [Kar00]. Converting from field linewidth to frequency linewidth one would expect FWHM$\sim$ 70 MHz for a single crystal. We observe a linewidth in Tab. 6.3 that is 2 orders of magntiude larger. We attribute this to the irregular shape of SrM and irregular clustering locally modifying H_{eff} in any of the NPs.

We assume that NPs form clusters with also randomly distributed anisotropy axis thereby we explain the large linewidth.

Detection of microwave excited spin waves by BLS

A microwave signal is injected into one CPW.

The microwave power is set to -10 dBm. The frequency is varied from 4.5 to 4.7 GHz. BLS data are taken at six different spots along the CPW, three sample points per each side of the CPW (Fig. 6.9).

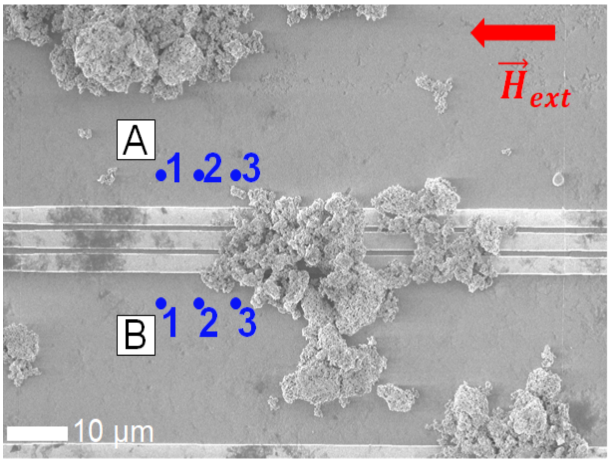

Figure 6.9: SEM image of strontium ferrite deposited on YIG. Strontium ferrite cluster is observed on the CPW. Red arrow indicates the direction of the applied static field. At positions A1 to A3 and B1 to B3 spectra were taken. Letters and number labelling refers to data plots in Fig. 6.10

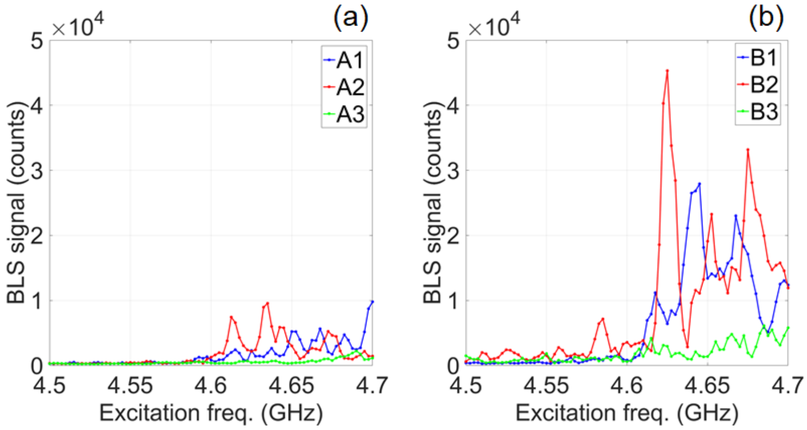

Figure 6.10: Microwave excited spin waves are detected by BLS from positions shown in Fig. 6.9. The integrated BLS signal (see section 3.2.3) is studied as function of the frequency of the microwave signal. The applied magnetic field is 100 mT, its direction is indicated in Fig. 6.9

In Fig. 6.10(a) we display data taken at positions A1 to A3 and in Fig. 6.10(b) data taken at positions B1 to B3. By comparison of plots in Fig. 6.10 nonreciprocal propagation is highlighted.

We attribute the absence of a resonance peak in the spectra taken at A3 and B3 to the enhanced spin wave scattering due to the influence of SrM cluster's stray field.

Kalinikos Slavin (KS) model for the first in plane resonant wavevector k_1 predicts $f_1 = 4.78$ GHz, adopting the estimated M_{eff} and $\frac{\gamma}{2\pi}$ values for sample YIG1-SrM. In KS model we used the wave vector we evaluated in section 4.2 to fit the first resonant mode in the RF field distribution of the CPW with $W_S = 2.9\,\mu$m.

In Fig. 6.10(b) the most prominent peak occur at 4.63 GHz. This value deviates from the theoretical value predicted by KS model ($f_1 = 4.78$) by 3%.

Factors that determine this discrepancy between measured resonant frequency and predicted one could be the following. (i) The width of the signal line along the CPW may be not constant. This deviates from the ideal profile that we simulated in Fig. 4.3; from FFT analysis of the RF field distribution (Fig. 4.4, black curve) we could expect that at resonance a narrow interval of wave vectors is excited because of the non-zero FWHM of the peak. (ii) The field calibration for BLS measurement can provide estimation of the field values within ±2 mT interval, this could led to slight change between nominally applied field and actual field thus leading to the observation of a resonance frequency shift. (iii) According to the formalism of [Aha00] we calculated the demagnetization factor along the direction of the applied field: $\mathrm{N}_z = 0.0019$, to take this effect into account in KS model.

Using these proposed reasons for mismatch between measured and predicted frequency one can assume that the applied is 98 mT instead of 100 mT calculate the resonance frequency considering demagnetizing effect. Considering demagnetization $H_{\text{ext}} = [98 - (0.0019 \cdot 171.9)]$ mT$=$ 97.7 mT, where $M_{\text{S}} = 171.9$ mT is assumed to be the effective magnetization that is estimated for sample YIG1-SrM.

From the resonant peak of the RF field distribution with the in-plane wave vector (Fig. 4.4) one can calculate: $k_1' = k_1 - (\text{FWHM}/2) = (0.368 \pm 0.002)$ rad/μm and assume that this is the minimum wave vector that contributes to the linewidth of the resonance peak.

Using the new parameters that have been calculated for H_{ext} and k_1' the first resonance mode according to Kalinikos Slavin model occurs at $f_1' = 4.66$ GHz.

The new computed value f_1' for resonance frequency of the first mode is closer to the measured value 4.63 GHz (relative error $\lesssim 1\%$), this justifies the reasons the we proposed to explain the observed mismatch between theoretical and measured value for resonance frequency of the lowest mode.

BLS measurement with a microwave power $= -5$ dBm and excitation frequency from 4.67 to 4.8 GHz are presented (Fig. 6.11). Data were taken as indicated in Fig. 6.10.

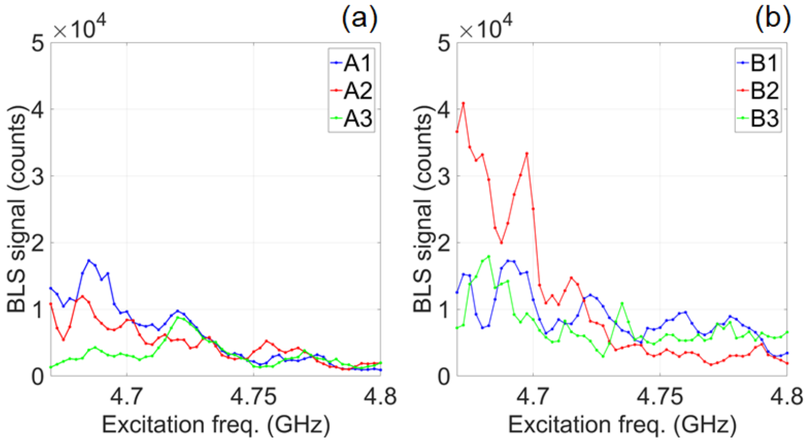

Figure 6.11: Microwave excited spin waves are detected by BLS from positions shown in Fig. 6.9. The integrated BLS signal (see section 3.2.3) is studied as function of the frequency of the microwave signal. The applied magnetic field is 100 mT, its direction is indicated in Fig. 6.9

In Fig. 6.11 we observe a resonance at positions A3 and A1 at 4.72 GHz. This suggests that increasing microwave signal power spin wave can be locally measured on SrM cluster.

Back side illumination
In backside illumation geometry light comes from the bottom layer of the chip, i.e. the GGG substrate.

BLS on thermally excited magnetization dynamics

The thermally excited magnetization dynamics is probed at 200 mT (Fig. 6.12(a)) and at 14 mT (Fig. 6.12(b)). Raw signals are then smoothed with a moving average window. The obtained signal is fitted to extract frequencies of the observed peaks Fig. 6.12(c),(d).

Laser power was set to 1 mW.

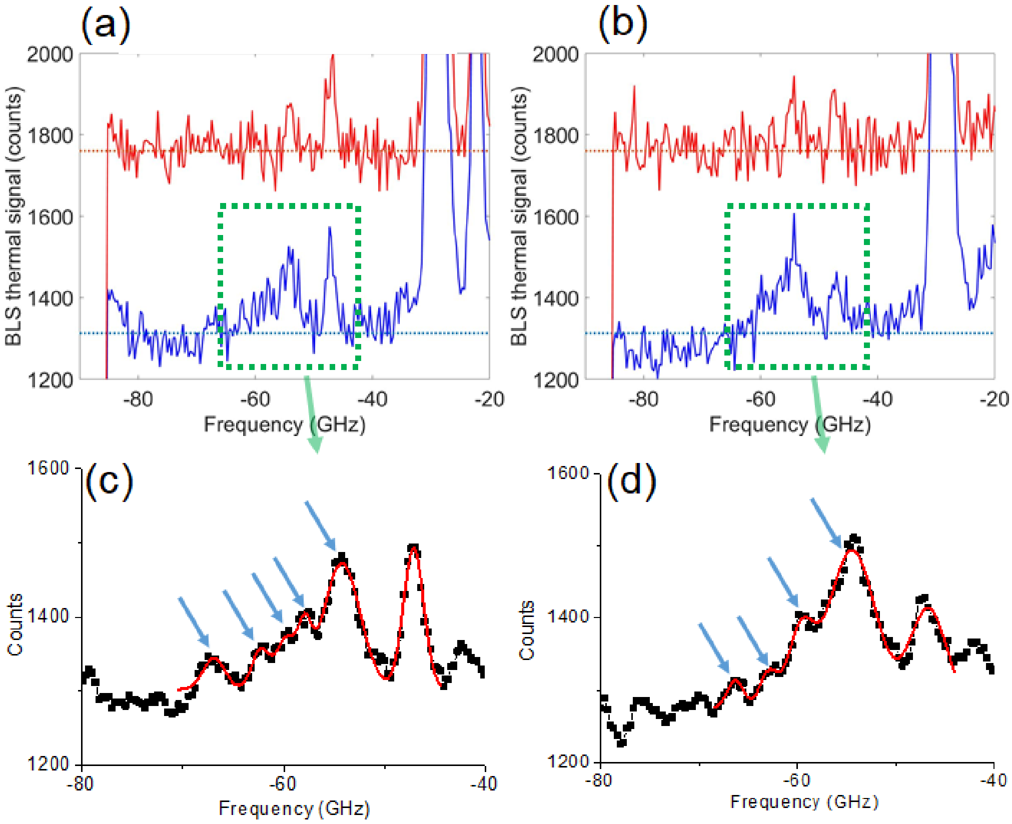

Figure 6.12: (a),(b) Thermal spectra of bare YIG (red solid curve) and of SrM cluster (blue solid curve). Horizontal lines are mean background values calculated in each case averaging the counts from minimum frequency up to -70 GHz. (a) Static magnetic field = 200 mT, (b) Static magnetic field = 14 mT. (c),(d) Multipeak gaussian fit is conducted after smoothing the raw data. For better convergence of the fit the laser peak (at ∼ 48 GHz) is also included in the analysis.

We assume random distribution of anisotropy axes within single SrM cluster. In comparison with data in Fig. 6.8 we remark that in Fig. 6.12 data are acquired pointing the laser on a different SrM cluster. We therefore consider a possible variation of the angle between applied field and anisotropy axes. This parameter is important to determine resonance condition as highlighted by the distribution fuction of resonance field strength in section 2.3.2. The shape change of the resonant curve in the thermally induced magnetization dynamics could be given by a different alignment of the grains within the cluster with respect to the applied field. According to the values of the high-order anisotropy constants peaks can occur in correspondence to resonance in along easy axis and hard axis as the external field is varied [Sch02], [Sch01].

In Tab. 6.4 fitted values of frequency and FWHM are reported for most important peak of those attributed to SrM cluster in Fig. 6.12. This peak has comparable central frequency to the lowest peak that is reported in Tab. 6.3. Due to the large FWHM they could belong to the same thermally excited resonance. This could suggest that we are able to always one mode of the thermally induced magnetization dynamics and that higher modes may vary according to the applied field and the orientation of the anisotropy axis according to theory (section 2.3.2).

Static field (mT)	$\|f\|$ (GHz)	σ_f (GHz)	Δf (GHz)	$\sigma_{\Delta f}$ (GHz)
14	54.5	0.1	4.0	0.2
200	54.2	0.1	3.6	0.2

Table 6.4: Central frequency and Full Width at Half Maximum (FWHM). $\Delta f$and is the FWHM of resonance f. Statistic errors from fit are reported as σ_f for peak frequency and as $\sigma_{\Delta f}$ for FWHM.

.

Summary on strontium ferrite decorated YIG

Experimental results show evidence of linewidth broadening and damping of propagating SWs. We attribute these observations to scattering of SWs due to strontium ferrite's stray field.

6.2 Samples YIG2 & YIG2-γFe$_2$O$_3$

We present VNA-AESWS spectra that are acquired in Damon-Eshbach excitation geometry. Microwave power for VNA measurement is set to -15 dBm.

6.2.1 VNA measurements - YIG2 & YIG2-γFe$_2$O$_3$

Magnetostatic surface wave mode excitation

In Fig. 6.13 S_{11} spectra for samples YIG2 and YIG2-γFe$_2$O$_3$ are shown.

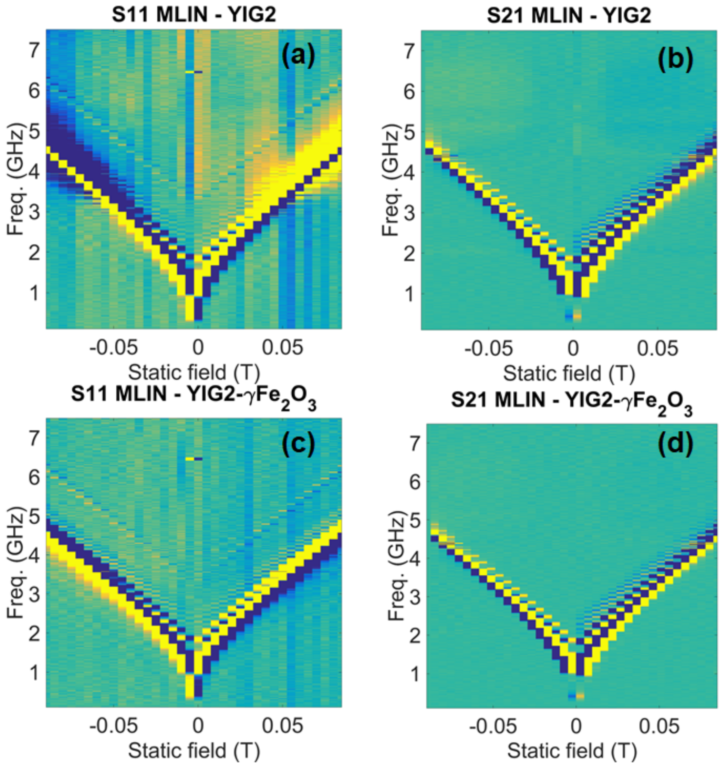

Figure 6.13: Color coded graphs showing (a) δS_{11} and (b) δS_{21} obtained on bare YIG: sample YIG2; (c) δS_{11} and (d) δS_{21} obtained on YIG decorated with SrM NPs: sample YIG2-γFe_2O_3. Signals. In (b) we observe non-reciprocity i.e. for $H > 0$ more resonant mode, propagating between the CPWs, are found compared to $H < 0$.

Comparing Fig. 6.13(b),(d) we do not observe reduction in transmitted signal for sample YIG2 and sample YIG2-γFe_2O_3. Eq. 2.56 is used to fit the PSSW resonance with n=1. In Fig. 6.14 PSSW formula is plotted for two values of exchange constant: 3.65 and 4 pJ/m.

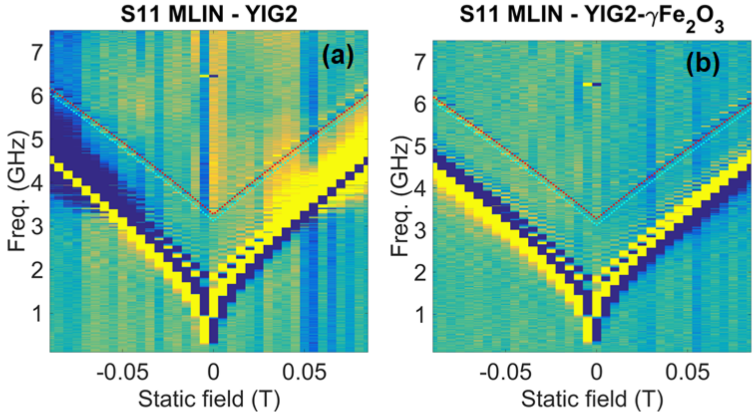

Figure 6.14: Color coded graphs showing (a) δS_{11} for sample YIG2 and (b) δS_{11} obtained for sample YIG2-γFe_2O_3. Cyan dotted line represents PSSW formula for $A_{\text{ex}} = 3.65$ pJ/m. Red dotted line represents PSSW resonance for $A_{\text{ex}} = 4$ pJ/m.

M_{eff} and $\frac{\gamma}{2\pi}$ are extracted from S_{11} measured data (see Tab. 6.5) as we have done in section 6.1. .

Parameter	YIG2	YIG2-γFe$_2$O$_3$
$\frac{\gamma}{2\pi}$ (GHz/T)	29.5 ± 0.7	29.5 ± 0.5
M_{eff} (mT)	173.7 ± 6.2	173.5 ± 5.0

Table 6.5: $\frac{\gamma}{2\pi}$ and M_{eff} parameters are fitted from S_{11} spectra. Lorentzian fit function is used for first resonant mode.

.

A large value for $\gamma/(2\pi)$ may be caused by a deviation of the actual applied field from the nominally field value. This mismatch between nominally and applied field does not influence our analysis of linewidth. We fit the resonant peaks to estimate their central frequency and their FWHM. Field mismatch is already taken into account when estimating the resonance frequency.

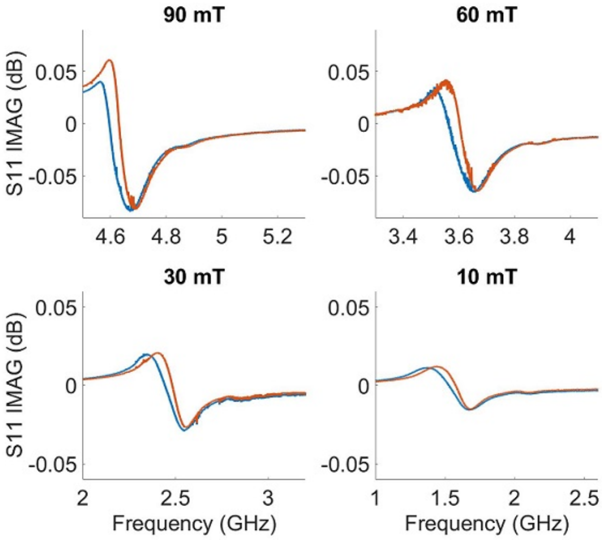

Figure 6.15: Imaginary part of reflection parameter S_{11} for selected static fields. Comparison between sample YIG2 (blue solid lines) and sample YIG2-γFe$_2$O$_3$ (red solid lines).

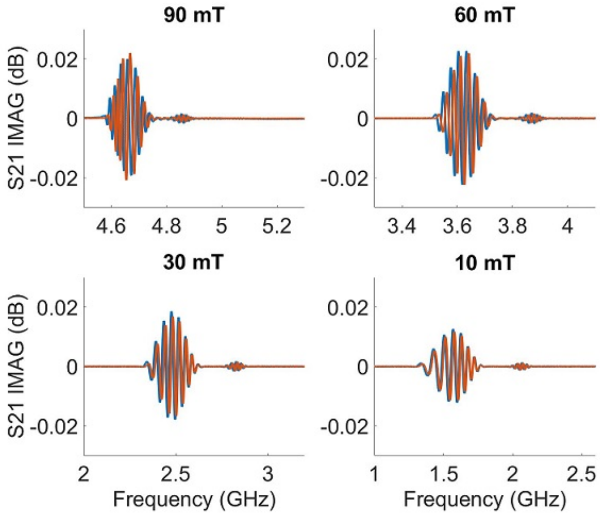

Figure 6.16: Imaginary part of transmission parameter S_{21} for selected static fields. Comparison between sample YIG2 (blue solid lines) and sample YIG2-γFe_2O_3 (red solid lines).

From Fig.s 6.15, 6.16 we do not observe signal reduction in transmission. This could be likely determined by the low concentration of nanoparticles across the YIG mesa. SEM characterization shows that only contact pads are highly covered (Fig. 5.4).

The linewidth for first resonance MSSW mode (Fig. 6.17) decreases after deposition (sample YIG2-γFe_2O_3). 6.17. This effect is observed in both transmission and reflection.

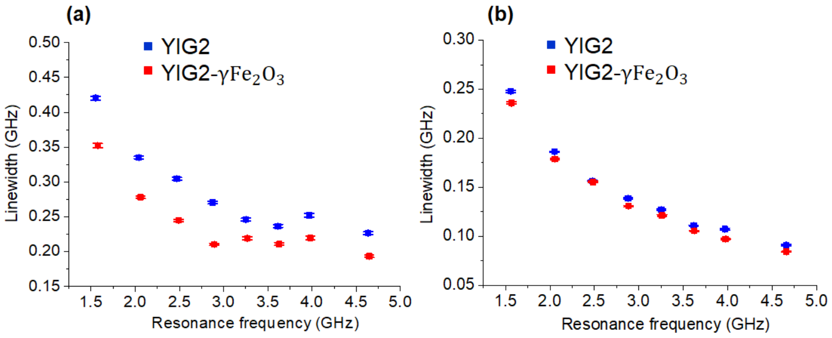

Figure 6.17: Linewidth for first resonance in magnetostatic surface mode configuration for (a) S_{11} and (b) S_{21} spectra.

For the 1^{st} PSSW mode the FWHM of the resonance peak is fitted as function of PSSW frequency in Fig. 6.19. A change in PSSW spectrum can be caused by a variation of boundary condition. Nanoparticles on YIG surface could potentially alter boundary condition. Fig. 6.18 shows the multipeak gaussian fit that is applied for δS_{11} at different fields.

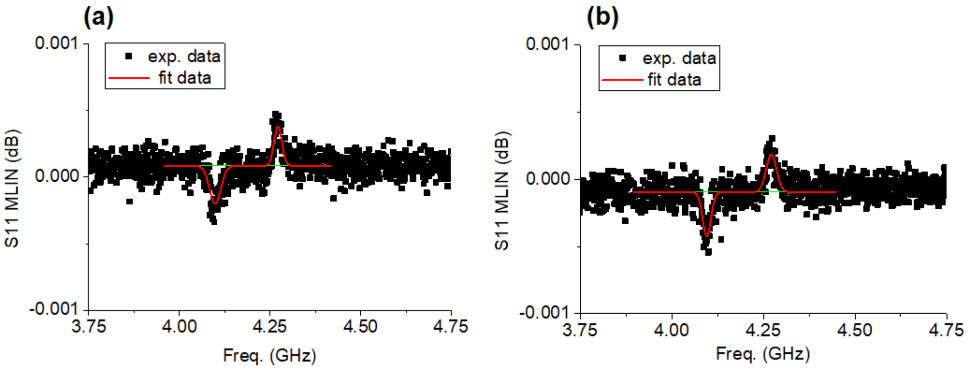

Figure 6.18: δS_{11} is reported (a) sample YIG2 and for (b) sample sample YIG2-γFe_2O_3.

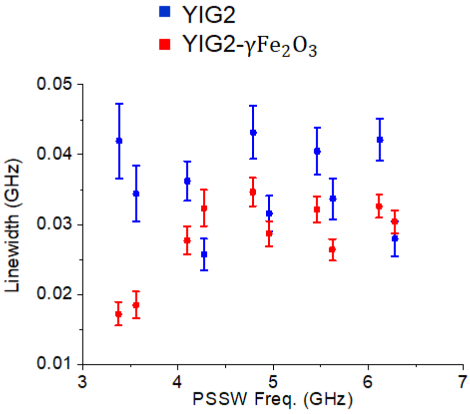

Figure 6.19: FWHM of PSSW resonance as function of PSSW frequency. Linewidth and PSSW frequency are both fitted from δS_{11}.

From Fig. 6.19 we observe a decrease of PSSW resonance linewidth for low frequency. Despite this observation it is not possible to draw a clear conclusion.

Summary on maghemite decorated YIG

We have presented VNA-AESWS investigation of YIG mesa decorated with superparamagnetic nanoparticles. This sample has not provided solid evidence of linewidth broadening.

We have observed high coverage of NPs on contact and taper region but not on the YIG mesa. The interesting outcome is related to the decrease of linewidth after deposition. This shows that the exposure of YIG to liquid do not deteriorate SW propagation properties. Further investigations are needed to evaluate the effect of maghemite particles.

7. Conclusions & Outlook

7.1 Summary

This thesis addresses one of the crucial challenges in magnonics: coupling microwaves to magnons. This is difficult due to wavelength mismatch. The magnonic grating coupler (MGC) effect has been an important discovery to excite spin wave featuring sub-100 nm wavelength. Magnetic nanoparticles (NPs) might be used as emitters or detectors in gratings. For this the interaction between spi nwaves and NPs needs to be evidenced. We have presented experimental data on strontium ferrite clusters and maghemite nanoparticles deposited on YIG supporting SWs.

With AFM characterization a typical height of the NPs of maghemite that decorated the CPW agreed with average size of NPs. For maghemite NPs the spin wave spectra did not allow to draw a clear conclusion. A linewidth decrease after deposition has been observed. A significant damping or signal strength reduction were not observed in transmission.

For strontium ferrite (SrM) decorated YIG spin wave spectra suggest enhanced damping of SWs in YIG. The linewidth increase of MSSW resonance is attributed to strontium ferrite stray field affecting spin wave resonance condition and spin wave propagation. The coupling of SrM clusters with magnons through the stray field could be compared with the MCG effect in [Yu02], as in that case the modulated stray field and magnetic susceptibility of the nanomagnet periodic array affected the spin wave excitation spectrum. In our case the effect of the stray field is not periodic and depends on strontium ferrite distribution over the YIG surface. As it is observed from BLS spectra extreme linewidth broadening can occur. From thermal spectra we can resolve the thermally excited magnetization dynamics of SrM. We interpret this as a spectrum typical of polycristalline materials featuring random anisotropy axes distribution.

What we observe can be interpreted as first experimental evidence that magnetic nanoparticles can act as magnetic scattering centers influencing spin waves' properties. With the results of this research activity interesting scientific points have been raised and they should be investigated in future work.

7.2 Possible future work

- *Nanomaterials preparation.* To reduce agglomeration the strontium ferrite suspension should be mechanically treated. The milling process would reduce the average size of the powder. Milling the suspension could be an efficient strategy as it is already known from related works [Zhu00]. This guarantees a more homogeneous decoration of YIG surface. Reducing the size of the magnetic scatterer is of crucial importance to enhance the efficiency of coupling between RF signal and short-waved magnons if used as transducer material.

- *Experimental setup.* Hexaferrite materials feature FMR frequency at $\gtrsim 50$ GHz at zero field. The direct excitation of magnetic resonance of these magnetic scatterers is interesting. A frequency multiplier is planned to be integrated in the microwave electronics of the BLS setup. This frequency multiplier will allow signals at ~ 70 GHz.

- *Micromagnetic simulation.* Micromagnetic simulations could offer further insight into the physics of the system and on its resonance behavior. This could ultimately enable to design a transducer based on NPs.

- *New device design.* Recently a new chip has been fabricated. Here nanoparticles are deposited on YIG before fabrication of microwave antennas. After lift off process the nanoparticles are only beneath coplanar waveguides. This is expected to enhance the interaction of nanoparticles with both microwave signal and excited spin waves.

8. Acknowledgements

I would like to express gratitude to all people that contributed to this work. In particular:

> Prof P. Bowen for his collaboration to prepare hexaferrite suspensions. He has allowed me to use his lab and tools. He has also taught me important lessons about chemical suspensions and ferrites materials.
>
> Prof. D. Grundler for offering me the possibility to work in his research group. His passion and excitement for scientific research have been a constant source of energy and inspiration for myself. I have truly appreciated his supervision, his expertise and his advice have been of crucial importance for this work. Interacting with him has also led to a personal growth, as I could learn from his explanations and suggestions.
>
> Prof. H. Hofmann and Dr. Markovic Milosevic for their support regarding maghemite suspension preparation. They provided me with their nanoparticle suspension, sharing with me valuable theoretical and practical knowledge on iron oxide based nanomaterials.
>
> Dr. K. An for his interest in my work. Interacting with him to discuss about VNA setup optimization and VNA data analysis has been always fruitful. His comments have helped improve the experimental data acquisition and stimulated further analysis on the results.
>
> Dr. V. S. Bhat for interesting discussion on micromagnetics and advice for VNA measurements.
>
> K. Baumgaertl for supervising my project on a daily basis and introducing me to LMGN laboratories. With patience and dedication he has always supported me by giving valuable assistance for experiments and technical issues that we encountered during this work. I should thank Korbinian for all interesting lessons about BLS and related experimental setup.
>
> P. Che for device fabrication and several scientific discussions. She has been always willing to interact with me whenever I had open questions. Ping also gave me important lessons on VNA-AESWS setup.
>
> M. C. Giordano for helping me with nanomaterials characterization. I have really appreciated her interest in my work and our discussion on suspension preparation and ferrites materials. Without her TEM and EDS characterization of strontium ferrite and maghemite nanoparticles could not have been possible.

M. Hamdi for interesting discussions over a broad range of topics in nanomagnetism. His curiosity and his wide knowledge have boosted my enthusiasm for this field.

A. Kúkol'ová for the very first TEM characterization of nanoparticles. Thanks to her I have been able to characterize the first nanoparticles suspension very soon after my arrival at LMGN. This has set the research of this thesis from the start on the correct track.

S. Watanabe for introducing me to LMGN AFM setup and patiently guiding me through my very first VNA-AESWS measurements. I appreciated our discussion as he has been always able to make important comments that help me improve my research.

I should thank E. Catapano for sharing with me the experience of being master's student at LMGN. In general working with LMGN group has been a great experience for me, from the interaction with such talented researchers I feel I have made a step further towards my professional growth.

I would like to thank my family for their unwavering trust in me and their constant emotional support.

Bibliography

[Agi00] Agilent Technologies,*Network Analyzer Basics*, (2000).

[Aha00] Aharoni, A. (1998). Demagnetizing factors for rectangular ferromagnetic prisms. *Journal of Applied Physics*, 83(6), pp.3432-3434.

[And00] D. Anderson, L. Smith, and J. Gruszynski: *S-Parameter Techniques for Faster, More Accurate Network Design, Hewlett Packard*, application note 95-1 edn. (1997).

[Ari00] Arias, R. and Mills, D. (2000). Extrinsic contributions to the ferromagnetic resonance response of ultrathin films. *Journal of Applied Physics*, 87(9), pp.5455-5456.

[Au00] Au, Y., Ahmad, E., Dmytriiev, O., Dvornik, M., Davison, T. and Kruglyak, V. (2012). Resonant microwave-to-spin-wave transducer. *Applied Physics Letters*, 100(18), p.182404.

[Bab00] Baberschke, K. (2011). Ferromagnetic resonance in nanostructures, rediscovering its roots in paramagnetic resonance. *Journal of Physics: Conference Series*, 324, p.012011..

[Bao00] Bao, M., Wong, K., Khitun, A., Lee, J., Hao, Z., Wang, K., Lee, D. and Wang, S. (2008). Determining wave vector and material property from the phase-shift of spin-wave propagation. *EPL (Europhysics Letters)*, 84(2), p.27009.

[Ben00] Ben Youssef, J., Vukadinovic, N., Billet, D. and Labrune, M. (2004). Thickness-dependent magnetic excitations in Permalloy films with nonuniform magnetization. *Physical Review B*, 69(17).

[Bil00] C. Bilzer: *Microwave susceptibility of thin ferromagnetic films: metrology and insight into magnetization dynamics*, Ph.D. thesis, Universite Paris-Sud 11 (2008).

[Blo00] F. Bloch, Z. Physik 61, 206 (1930); 74, 295 (1932).

[Bloe00] Bloembergen, N. and Wang, S. (1954). Relaxation Effects in Para- and Ferromagnetic Resonance. *Physical Review*, 93(1), pp.72-83.

[Blu00] S. Blundell: *Magnetism in Condensed Matter*, Oxford University Press, Oxford, 2001

[Bon00] Bonvin, D., Arakcheeva, A., Millán, A., Piñol, R., Hofmann, H. and Mionić Ebersold, M. (2017). Controlling structural and magnetic properties of IONPs by aqueous synthesis for improved hyperthermia. *RSC Advances*, 7(22), pp.13159-13170.

[Bra00] Brataas, A., Nazarov, Y. and Bauer, G. (2000). Finite-Element Theory of Transport in Ferromagnet?Normal Metal Systems. *Physical Review Letters*, 84(11), pp.2481-2484.

[Bra01] Brataas, A., Tserkovnyak, Y., Bauer, G. and Halperin, B. (2002). Spin battery operated by ferromagnetic resonance. *Physical Review B*, 66(6).

[Bra02] Brataas, A., Tserkovnyak, Y. and Bauer, G. (2008). Scattering Theory of Gilbert Damping. *Physical Review Letters*, 101(3).

[Cao00] Cao, H., Zhao, Z., Lee, M., Choi, E., McGuire, M., Sales, B., Zhou, H., Yan, J. and Mandrus, D. (2015). High pressure floating zone growth and structural properties of ferrimagnetic quantum paraelectric BaFe12O19. *APL Materials*, 3(6), p.062512.

[Car00] Carva, K. and Turek, I. (2007). Spin-mixing conductances of thin magnetic films from first principles. *Physical Review B*, 76(10).

[Chu00] Chumak, A., Serga, A. and Hillebrands, B. (2017). Magnonic crystals for data processing. *Journal of Physics D: Applied Physics*, 50(24), p.244001.

[Chu01] Chumak, A., Serga, A. and Hillebrands, B. (2014). Magnon transistor for all-magnon data processing. *Nature Communications*, 5(1).

[Coc00] Cochran, J. and Dutcher, J. (1988). Calculation of the intensity of light scattered from magnons in thin films. *Journal of Magnetism and Magnetic Materials*, 73(3), pp.299-310.

[Dam00] R. W. Damon und J. R. Eshbach: Magnetostatic modes of a ferromagnetic slab, *J. Appl. Phys. 19*, 308 (1961).

[Dem00] Demidov, V. and Demokritov, S. (2015). Magnonic Waveguides Studied by Microfocus Brillouin Light Scattering. *IEEE Transactions on Magnetics*, 51(4), pp.1-15.

[Dem01] Demidov, V., Kostylev, M., Rott, K., Krzysteczko, P., Reiss, G. and Demokritov, S. (2009). Excitation of microwaveguide modes by a stripe antenna. *Applied Physics Letters*, 95(11), p.112509.

[Demo00] Demokritov, S. (2001). Brillouin light scattering studies of confined spin waves: linear and nonlinear confinement. *Physics Reports*, 348(6), pp.441-489.

[DeW00] De Wames, R. and Wolfram, T. (1970). Dipole−Exchange Spin Waves in Ferromagnetic Films. *Journal of Applied Physics*, 41(3), pp.987-993.

[Dys00] Dyson, F. (1956). General Theory of Spin-Wave Interactions. *Physical Review*, 102(5), pp.1217-1230.

[Ebb00] Ebbesen, T., Genet, C. and Bozhevolnyi, S. (2008). Surface-plasmon circuitry. *Physics Today*, 61(5), pp.44-50.

[Exl00] L. Exl, Intro *Micromagnetism*, preprint of book chapter, prefinal version 18 Sept. 2016, Retrieved from URL. Homepage.univie.ac.at. (2018). [online] Available at: http://homepage.univie.ac.at/lukas.exl/files/mic_intro.pdf [Accessed 18 Aug. 2018].

[Eur00] Eurenius, L., Hägglund, C., Olsson, E., Kasemo, B. and Chakarov, D. (2008). Grating formation by metal-nanoparticle-mediated coupling of light into waveguided modes. *Nature Photonics*, 2(6), pp.360-364.

[Faeh00] Fähnle, M. and Illg, C. (2011). Electron theory of fast and ultrafast dissipative magnetization dynamics. *Journal of Physics: Condensed Matter*, 23(49), p.493201.

[Fes00] Fesharaki, F., Hossain, N., Vigne, S., Chaker, M. and Wu, K. (2016). Accurate theoretical and experimental characterization of optical grating coupler. *Optics Express*, 24(18), p.21027.

[Fis00] Fischer, T., Kewenig, M., Bozhko, D., Serga, A., Syvorotka, I., Ciubotaru, F., Adelmann, C., Hillebrands, B. and Chumak, A. (2017). Experimental prototype of a spin-wave majority gate. *Applied Physics Letters*, 110(15), p.152401.

[Fra00] Franco, A., Zapf, V., Barbeta, V. and Jardim, R. (2010). Spin-wave fluctuations in ferrimagnetic $\mathrm{Mg}_x\mathrm{Fe}_{3-x}\mathrm{O4}$ nanoparticles. *Journal of Applied Physics*, 107(7), p.073904.

[Ger00] Gerrits, T., Schneider, M. and Silva, T. (2006). Enhanced ferromagnetic damping in Permalloy−Cu bilayers. *Journal of Applied Physics*, 99(2), p.023901.

[Gie00] F. Giesen: *Magnetization Dynamics of Nanostructured Ferromagnetic Rings and Rectangular Elements*, Ph.D. thesis, University Hamburg (2005).

[Gil00] T. Gilbert: *A Lagrangian Formulation of the Gyromagnetic Equation of the Magnetization Field*, Phys. Rev. 100, 1243 (1955).

[Gla00] Gladii, O., Haidar, M., Henry, Y., Kostylev, M. and Bailleul, M. (2016). Frequency nonreciprocity of surface spin wave in permalloy thin films. *Physical Review B*, 93(5).

[Gru00] Grundler, D. (2016). Nanomagnonics. Journal of Physics D: Applied Physics, 49(39), p.391002.

[Gur00] Gurevich, A. and Melkov, G. (2010). *Magnetization oscillations and waves*. Boca Raton: CRC Press.

[Hal00] Haldar, A., Kumar, D. and Adeyeye, A. (2016). A reconfigurable waveguide for energy-efficient transmission and local manipulation of information in a nanomagnetic device. *Nature Nanotechnology*, 11(5), pp.437-443.

[Han00] O'Handley, R. (2000). *Modern magnetic materials*. New York: John Wiley.

[Hei00] Heinrich, B., Urban, R. and Woltersdorf, G. (2002). Magnetic relaxation in metallic films: Single and multilayer structures. *Journal of Applied Physics*, 91(10), p.7523.

[Hau00] Hauser, C., Richter, T., Homonnay, N., Eisenschmidt, C., Qaid, M., Deniz, H., Hesse, D., Sawicki, M., Ebbinghaus, S. and Schmidt, G. (2016). Yttrium Iron Garnet Thin Films with Very Low Damping Obtained by Recrystallization of Amorphous Material. *Scientific Reports*, 6(1).

[Her00] C. Herring and C. Kittel, Phys. Rev. 81, 869 (1951).

[Hol00] T. Holstein and H. Primakoff, Phys. Rev. 58, 1098 (1940)

[Hub00] R. Huber: *Control of Spin Waves on the Nanoscale in One-Dimensional Magnonic Crystals and Atomic Layer Deposition of Metallic Ferromagnets for Second Generation of Nanomaterials*, Ph.D. thesis, Technical University Munich (2013).

[Hur00] Hurben, M. and Patton, C. (1998). Theory of two magnon scattering microwave relaxation and ferromagnetic resonance linewidth in magnetic thin films. *Journal of Applied Physics*, 83(8), pp.4344-4365.

[Kal00] Kalarickal, S., Mo, N., Krivosik, P. and Patton, C. (2009). Ferromagnetic resonance linewidth mechanisms in polycrystalline ferrites: Role of grain-to-grain and grain-boundary two-magnon scattering processes. *Physical Review B*, 79(9).

[Kali00] Kalinikos, B. and Slavin, A. (1986). Theory of dipole-exchange spin wave spectrum for ferromagnetic films with mixed exchange boundary conditions. *Journal of Physics C: Solid State Physics*, 19(35), pp.7013-7033.

[Kap00] Kapelrud, A. and Brataas, A. (2013). Spin Pumping and Enhanced Gilbert Damping in Thin Magnetic Insulator Films. *Physical Review Letters*, 111(9).

[Kar00] Karim, R., McKinstry, K., Truedson, J. and Patton, C. (1992). Frequency dependence of the FMR linewidth in single crystal barium ferrite platelets. *IEEE Transactions on Magnetics*, 28(5), pp.3225-3227.

[Kef00] Kefeni, K., Msagati, T. and Mamba, B. (2017). Ferrite nanoparticles: Synthesis, characterisation and applications in electronic device. *Materials Science and Engineering*: B, 215, pp.37-55.

[Kos00] Kostylev, M. (2013). Non-reciprocity of dipole-exchange spin waves in thin ferromagnetic films. *Journal of Applied Physics*, 113(5), p.053907.

[Key00] Keysight Technologies: *Understanding the Fundamental Principles of Vector Network Analysis*, application note. (2017)

[Key01] Keysight Technologies: *Specifying Calibration Standards and Kits for Keysight Vector Network Analyzers*, application note 1287-11.

[Key02] Keysight Technologies: *Applying Error Correction to Vector Network Analyzer Measurements*, application note 1287-3.

[Kit00] Kittel, C. (1948). On the Theory of Ferromagnetic Resonance Absorption. *Physical Review*, 73(2), pp.155-161.

[Khi00] Khivintsev, Y., Marsh, J., Zagorodnii, V., Harward, I., Lovejoy, J., Krivosik, P., Camley, R. and Celinski, Z. (2011). Nonlinear amplification and mixing of spin waves in a microstrip geometry with metallic ferromagnets. *Applied Physics Letters*, 98(4), p.042505.

[Koe00] Koev, S., Agrawal, A., Lezec, H. and Aksyuk, V. (2011). An Efficient Large-Area Grating Coupler for Surface Plasmon Polaritons. *Plasmonics*, 7(2), pp.269-277.

[Kra00] Krawczyk, M. and Grundler, D. (2014). Review and prospects of magnonic crystals and devices with reprogrammable band structure. *Journal of Physics: Condensed Matter*, 26(12), p.123202.

[Kra01] Krawczyk, M. and Puszkarski, H. (2008). Plane-wave theory of three-dimensional magnonic crystals. *Physical Review B*, 77(5).

[Lan00] D. L. Landau und E. Lifshitz: *On the theory of the dispersion of magnetic permeability in ferromagnetic bodies*, Phys. Z. Sowjetunion 8 (1935).

[Lee00] Lee, H., Schulthess, T., Landau, D., Brown, G., Pierce, J., Gai, Z., Farnan, G. and Shen, J. (2002). Monte Carlo simulations of interacting magnetic nanoparticles. *Journal of Applied Physics*, 91(10), p.6926.

[Li00] Li, X., Labanowski, D., Salahuddin, S. and Lynch, C. (2017). Spin wave generation by surface acoustic waves. Journal of Applied Physics, 122(4), p.043904.

[Lin00] Lindner, J., Lenz, K., Kosubek, E., Baberschke, K., Spoddig, D., Meckenstock, R., Pelzl, J., Frait, Z. and Mills, D. (2003). Non-Gilbert-type damping of the magnetic relaxation in ultrathin ferromagnets: Importance of magnon-magnon scattering. *Physical Review B*, 68(6).

[Liu00] Liu, C., Chen, J., Liu, T., Heimbach, F., Yu, H., Xiao, Y., Hu, J., Liu, M., Chang, H., Stueckler, T., Tu, S., Zhang, Y., Zhang, Y., Gao, P., Liao, Z., Yu, D., Xia, K., Lei, N., Zhao, W. and Wu, M. (2018). Long-distance propagation of short-wavelength spin waves. *Nature Communications*, 9(1).

[Mae00] Maendl, S., Stasinopoulos, I. and Grundler, D. (2017). Spin waves with large decay length and few 100−nm wavelengths in thin yttrium iron garnet grown at the wafer scale. *Applied Physics Letters*, 111(1), p.012403.

[Mei00] Meindl, J. (2001). Limits on Silicon Nanoelectronics for Terascale Integration. *Science*, 293(5537), pp.2044-2049.

[Mel00] Melkov, G., Kobljanskyj, Y., Serga, A., Tiberkevich, V. and Slavin, A. (2001). Reversal of Momentum Relaxation. *Physical Review Letters*, 86(21), pp.4918-4921.

[Mit00] Mitsumata, C. and Tomita, S. (2011). Control of Gilbert damping using magnetic metamaterials. *Physical Review B*, 84(17).

[Mru00] Mruczkiewicz, M., Krawczyk, M., Sakharov, V., Khivintsev, Y., Filimonov, Y. and Nikitov, S. (2013). Standing spin waves in magnonic crystals. *Journal of Applied Physics*, 113(9), p.093908.

[Mru01] Mruczkiewicz, M., Krawczyk, M., Gubbiotti, G., Tacchi, S., Filimonov, Y., Kalyabin, D., Lisenkov, I. and Nikitov, S. (2013). Nonreciprocity of spin waves in metallized magnonic crystal. *New Journal of Physics*, 15(11), p.113023.

[Neu00] S. Neusser: *Spin Waves in Antidot Lattices: From Quantization to Magnonic Crystals*, Ph.D. thesis, Technical University Munich (2011).

[Osb00] Osborn, J. (1945). Demagnetizing Factors of the General Ellipsoid. *Physical Review*, 67(11-12), pp.351-357.

[Pap00] Papaefthymiou, G. (2009). Nanoparticle magnetism. *Nano Today*, 4(5), pp.438-447.

[Pol00] Polder, D. (1949). On the theory of ferromagnetic resonance. *Physica*, 15(1-2), pp.253-255.

[Poz00] Pozar, D. (2012). *Microwave engineering.* Hoboken, N.J.: Wiley.

[Pul00] Pullar, R. (2012). Hexagonal ferrites: A review of the synthesis, properties and applications of hexaferrite ceramics. *Progress in Materials Science*, 57(7), pp.1191-1334.

[Rop00] Ropers, C., Neacsu, C., Elsaesser, T., Albrecht, M., Raschke, M. and Lienau, C. (2007). Grating-Coupling of Surface Plasmons onto Metallic Tips: A Nanoconfined Light Source. *Nano Letters*, 7(9), pp.2784-2788.

[Sav00] Savochkin, I., Jäckl, M., Belotelov, V., Akimov, I., Kozhaev, M., Sylgacheva, D., Chernov, A., Shaposhnikov, A., Prokopov, A., Berzhansky, V., Yakovlev, D., Zvezdin, A. and Bayer, M. (2017). Generation of spin waves by a train of fs-laser pulses: a novel approach for tuning magnon wavelength. *Scientific Reports*, 7(1).

[Sch00] Schlömann, E. (1958). Spin-wave analysis of ferromagnetic resonance in polycrystalline ferrites. *Journal of Physics and Chemistry of Solids*, 6(2-3), pp.242-256.

[Sch01] Schlömann, E. (1958). Ferromagnetic resonance in polycrystalline ferrites with large anisotropy—I. *Journal of Physics and Chemistry of Solids*, 6(2-3), pp.257-266.

[Sch02] Schlömann, E. and Jones, R. (1959). Ferromagnetic Resonance in Polycrystalline Ferrites with Hexagonal Crystal Structure. *Journal of Applied Physics*, 30(4), pp.S177-S178.

[Schw00] T. Schwarze: *SpinWaves in 2D and 3D Magnonic Crystals: From Nanostructured Ferromagnetic Materials to Chiral Helimagnets*, Ph.D. thesis, Technical University Munich (2013).

[Seb00] Sebastian, T., Schultheiss, K., Obry, B., Hillebrands, B. and Schultheiss, H. (2015). Micro-focused Brillouin light scattering: imaging spin waves at the nanoscale. *Frontiers in Physics*, 3.

[She00] Shen, Y. and Bloembergen, N. (1966). Interaction between Light Waves and Spin Waves. *Physical Review*, 143(2), pp.372-384.

[Shi00] Shilov, V., Bacri, J., Gazeau, F., Gendron, F., Perzynski, R. and Raikher, Y. (1999). Ferromagnetic resonance in ferrite nanoparticles with uniaxial surface anisotropy. *Journal of Applied Physics*, 85(9), pp.6642-6647.

[Shi01] Shilov, V., Raikher, Y., Bacri, J., Gazeau, F. and Perzynski, R. (1999). Effect of unidirectional anisotropy on the ferromagnetic resonance in ferrite nanoparticles. Physical Review B, 60(17), pp.11902-11905.

[Sta00] D. D. Stancil und A. Prabhakar: *Spin Waves: Theory and Applications*, Springer, 2009.

[Sto00] J. Stoehr und H. C. Siegmann: Magnetism - From Fundamentals to Nanoscale Dynamics, Springer, Berlin, 2006

[Suk00] Sukhov, A., Usadel, K. and Nowak, U. (2008). Ferromagnetic resonance in an ensemble of nanoparticles with randomly distributed anisotropy axes. *Journal of Magnetism and Magnetic Materials*, 320(1-2), pp.31-35.

[Tab00] THE TABLE STABLE LTD., *HIGH CONTRAST TANDEM FABRY-PÉROT INTERFEROMETER TFP−2 HC*, operator manual.

[Tan00] Seavey, M. and Tannenwald, P. (1958). Direct Observation of Spin-Wave Resonance. *Physical Review Letters*, 1(5), pp.168-169.

[Tse00] Tserkovnyak, Y., Brataas, A. and Bauer, G. (2002). Enhanced Gilbert Damping in Thin Ferromagnetic Films. *Physical Review Letters*, 88(11).

[Ver00] Verba, R., Carpentieri, M., Finocchio, G., Tiberkevich, V. and Slavin, A. (2016). Excitation of propagating spin waves in ferromagnetic nanowires by microwave voltage-controlled magnetic anisotropy. *Scientific Report*, 6(1).

[Vla00] Vlaminck, V. and Bailleul, M. (2010). Spin-wave transduction at the submicrometer scale: Experiment and modeling. Physical Review B, 81(1).

[Vog00] Vogel, M., Chumak, A., Waller, E., Langner, T., Vasyuchka, V., Hillebrands, B. and von Freymann, G. (2015). Optically reconfigurable magnetic materials. *Nature Physics*, 11(6), pp.487-491.

[Vogt00] Vogt, K., Fradin, F., Pearson, J., Sebastian, T., Bader, S., Hillebrands, B., Hoffmann, A. and Schultheiss, H. (2014). Realization of a spin-wave multiplexer. *Nature Communications*, 5(1).

[Wad00] Wadell, B. (2003). *Transmission line design handbook.* Boston: Artech House.

[Wal00] Walker, L. (1957). Magnetostatic Modes in Ferromagnetic Resonance. *Physical Review*, 105(2), pp.390-399.

[Wet00] Wettling, W., Cottam, M. and Sandercock, J. (1975). The relation between one-magnon light scattering and the complex magneto-optic effects in YIG. *Journal of Physics C: Solid State Physics*, 8(2), pp.211-228.

[Wor00] Worthing, P. and Barnes, W. (2001). Efficient coupling of surface plasmon polaritons to radiation using a bi-grating. *Applied Physics Letters*, 79(19), pp.3035-3037.

[Yu00] Yu, H., Huber, R., Schwarze, T., Brandl, F., Rapp, T., Berberich, P., Duerr, G. and Grundler, D. (2012). High propagating velocity of spin waves and temperature dependent damping in a CoFeB thin film. *Applied Physics Letters*, 100(26), p.262412.

[Yu01] Yu, H., d Allivy Kelly, O., Cros, V., Bernard, R., Bortolotti, P., Anane, A., Brandl, F., Heimbach, F. and Grundler, D. (2016). Approaching soft X-ray wavelengths in nanomagnet-based microwave technology. *Nature Communications*, 7, p.11255.

[Yu02] Yu, H., Duerr, G., Huber, R., Bahr, M., Schwarze, T., Brandl, F. and Grundler, D. (2013). Omnidirectional spin-wave nanograting coupler. *Nature Communications*, 4(1)

[Yu03] Yu H. and D. Grundler, *Spin-wave Spectroscopy on Ferromagnetic Thin Film Using Vector Network Analyzer*, Technical University Munich, (2013).

[Zhu00] Zhuravlev, V., Minin, R., Itin, V., Lopushnyak, Y., Zhuravlev, A. and Lilenko, E. (2017). Study of the magnetic anisotropy of the multiphase samples of the ferrimagnets with hexagonal crystal structure by the method of ferromagnetic resonance. *IOP Conference Series: Materials Science and Engineering*, 168, p.012081.